



**POLITECNICO**  
MILANO 1863

SCUOLA DI INGEGNERIA INDUSTRIALE  
E DELL'INFORMAZIONE

# Design of a Compliance-Controlled Chamber for an Aortic Phantom: Hyperelastic Characterization and Windkessel Analysis

TESI DI LAUREA MAGISTRALE IN  
BIOMEDICAL ENGINEERING - INGEGNERIA BIOMEDICA

Author: **Seyed Mahdi Hoseinkhah**

Student ID: 10831486

Advisor: Prof. Emiliano Votta

Co-advisors: Dr. Francesco Sturla

Academic Year: 2024-2025



# Abstract

The aorta is the most compliant vessel in the body. Accurate replication of physiological aortic compliance is essential in experimental cardiovascular modeling. The aorta's flexible wall not only enables proper hemodynamic function but also serves as an indicator of cardiovascular health and potential pathology.

This thesis presents the design and characterization of a compliance-controlled chamber hosting an aortic phantom within a sealed air–water system. The goal is to mimic physiological compliance by regulating the external pressure applied to the phantom. A hyperelastic constitutive model based on the Mooney–Rivlin formulation is used to describe the mechanical behavior of the aortic wall, and theoretical stress–strain relationships are derived to evaluate changes in volume and diameter under dynamic pressure conditions.

The chamber is specifically optimized to reproduce physiological distensibility by tuning external boundary conditions. This setup is capable of achieving physiological compliance and supporting both steady and pulsatile flow regimes. Finally, a Windkessel-based lumped parameter model is developed to provide a first-order estimation of the phantom's hemodynamic performance and pressure–flow characteristics.

**Keywords:** Aortic phantom, Hyperelastic analysis, Compliance chamber, Windkessel model, Arterial compliance In vitro cardiovascular system



## Abstract in lingua italiana

L'aorta è il vaso più compliant del corpo umano. Una riproduzione accurata della compliance fisiologica dell'aorta è fondamentale nella modellazione cardiovascolare sperimentale. La parete flessibile dell'aorta non solo consente un corretto funzionamento emodinamico, ma rappresenta anche un indicatore dello stato di salute cardiovascolare e di potenziali patologie.

Questa tesi presenta la progettazione e la caratterizzazione di una camera a compliance controllata, in grado di ospitare un fantoccio aortico all'interno di un sistema sigillato ad aria e acqua. L'obiettivo è imitare la compliance fisiologica regolando la pressione esterna applicata al fantoccio. Un modello costitutivo iperelastico basato sulla formulazione di Mooney–Rivlin è utilizzato per descrivere il comportamento meccanico della parete aortica, e vengono derivate relazioni teoriche sforzo–deformazione per valutare le variazioni di volume e diametro in condizioni di pressione dinamica.

La camera è specificamente ottimizzata per riprodurre la distensibilità fisiologica tramite la regolazione delle condizioni al contorno esterne. Il sistema è in grado di raggiungere la compliance fisiologica e di supportare sia flussi stazionari che pulsati. Infine, viene sviluppato un modello lumped parameter basato su Windkessel per fornire una stima di primo ordine delle prestazioni emodinamiche e delle caratteristiche pressione-flusso del fantoccio.

**Parole chiave:** Fantoccio aortico, Modellazione iperelastica, Camera a compliance controllata, Modello di Windkessel, Compliance arteriosa, Sistema cardiovascolare in vitro



# Contents

<b>Abstract</b>	<b>i</b>
<b>Abstract in lingua italiana</b>	<b>iii</b>
<b>Contents</b>	<b>v</b>
<b>1 Introduction</b>	<b>1</b>
1.1 Aortic Compliance: Physiological Basis and Metrics . . . . .	1
1.2 Problem Statement: Limitations of Existing In Vitro Compliance Models . . . . .	2
1.3 Research Objectives . . . . .	3
1.4 Thesis Structure . . . . .	4
<b>2 Literature Review</b>	<b>5</b>
2.1 Aorta . . . . .	5
2.1.1 Anatomy of the Aorta . . . . .	5
2.1.2 Pathology . . . . .	9
2.2 Compliance and distensibility . . . . .	13
2.2.1 Compliance and its role in cardiovascular modeling . . . . .	13
2.2.2 state of art . . . . .	15
<b>3 Materials and Methods</b>	<b>21</b>
3.1 Overall workflow . . . . .	21
3.2 Mathematical modelling . . . . .	22
3.2.1 Constitutive Equation . . . . .	22
3.2.2 Thin-wall Hoop Stress for Cylindrical Tube . . . . .	25
3.2.3 Definition of Internal and External Pressure . . . . .	26
3.3 Modeling the Circulatory Loop Using a Windkessel Approach . . . . .	28
3.4 Windkessel Equation Formulation . . . . .	30
3.4.1 Experimental R-C Parameters in Human Systemic Arterial Models	33

3.5	Pressure waive and its effect on compliance . . . . .	36
3.6	Imaging and 3D Printing of the Aortic Phantom . . . . .	37
3.6.1	Imaging and segmentation . . . . .	37
3.6.2	Anatomical Variation in Aortic Morphology . . . . .	40
3.6.3	3D Printing of the Aortic Phantom . . . . .	41
<b>4</b>	<b>Results</b>	<b>45</b>
4.1	Governing Equation Overview . . . . .	45
4.2	Compliance and Distensibility . . . . .	46
4.2.1	Simulation Parameters and Definitions . . . . .	47
4.2.2	Variation of Compliance with diastolic-systolic pressure . . . . .	48
4.2.3	Distensibility Response to Arterial Pressure . . . . .	50
4.2.4	Circumferential Stretch Ratio ( $\lambda$ ) as a Function of Pump Pressure .	52
4.3	Design of the Compliance-Controlled Chamber . . . . .	53
4.3.1	Inlet-Outlet and sensors Configuration . . . . .	55
4.3.2	Lid Design and Sealing Mechanism . . . . .	57
4.4	Circulatory Hemodynamic Analysis Via LPM Modeling . . . . .	59
4.4.1	Decomposition of Total Resistance Components . . . . .	59
<b>Bibliography</b>		<b>65</b>
<b>A Appendix A: Governing C1 and C2 from the uniaxial test</b>		<b>71</b>
Appendix A: Fitting Mooney–Rivlin Constants to Uniaxial Test Data . . . . .		71
<b>List of Figures</b>		<b>73</b>
<b>List of Tables</b>		<b>75</b>
<b>Acknowledgements</b>		<b>77</b>

# 1 | Introduction

## 1.1. Aortic Compliance: Physiological Basis and Metrics

The aorta, as a large elastic artery, plays a critical role in dampening the pulsatile output of the heart and transforming it into a steady flow through the arterial system[19]. This cushioning effect, commonly described by the Windkessel mechanism, allows the aortic wall to temporarily store blood during systole and release it during diastole, thereby maintaining continuous perfusion of the organs[1][2]. The Windkessel effect is crucial for protecting downstream microcirculation from excessive pressure fluctuations, ensuring that delicate capillaries are not exposed to harmful pulsatile stresses[3]. In essence, the inherent compliance of the aorta (its ability to expand with pressure) serves as a physiologic buffer that stabilizes blood flow and pressure throughout the cardiac cycle.

Aortic compliance is quantitatively expressed through metrics such as aortic distensibility and compliance coefficient, which measure the vessel's deformability under changing pressure. Distensibility ( $D$ ) is typically defined as the fractional change in cross-sectional area per unit pressure change. In clinical practice, non-invasive imaging modalities like cardiovascular MRI and CT, combined with blood pressure measurements, are used to assess these parameters by capturing the aortic diameter or area in systole and diastole[33][39]. A healthy aorta exhibits high distensibility, meaning it enlarges appreciably with the pulse pressure, whereas a stiffened aorta shows only minimal expansion for the same pressure. Importantly, aortic distensibility is inversely related to pulse wave velocity (PWV): stiffer (less compliant) vessels transmit pressure waves faster, making PWV a surrogate measure of arterial stiffness. Reduced aortic elasticity – manifested as low distensibility and high PWV – is recognized as an early indicator of arterial aging and pathology. For example, studies have shown that increased aortic compliance can improve cardiac performance by reducing the left ventricular afterload. Conversely, a loss of compliance (increased stiffness) is associated with elevated pulse pressures and is an independent predictor of cardiovascular morbidity and mortality[23]. These facts underscore that physiological aor-

tic compliance is essential not only for efficient hemodynamics but also as a marker of cardiovascular health. Any realistic cardiovascular model, therefore, must replicate the compliant behavior of the aorta to accurately reflect *in vivo* conditions.

## 1.2. Problem Statement: Limitations of Existing In Vitro Compliance Models

Despite the vital importance of aortic compliance, replicating this behavior *in vitro* remains challenging. Many experimental cardiovascular setups rely on rigid aortic phantoms for simplicity and clarity in flow visualization[11]. In such benchtop mock circulatory loops, compliance is often introduced by external elements (e.g. air-filled chambers or elastic bags) rather than by the phantom itself[31]. While this approach can simulate overall arterial compliance in the flow circuit, the distributed compliance of the aorta is not inherently captured by a rigid tube. On the other hand, flexible aortic phantoms made of silicone or other elastomers have been developed to mimic the vessel's deformability. However, manufacturing soft phantoms with truly physiological mechanical properties is notoriously difficult. Techniques like silicone dipping or casting are sensitive to factors such as curing temperature, humidity, and mold design, often resulting in models whose stiffness may not precisely match that of real aortic tissue[49]. Consequently, even if the phantom's geometry is anatomically accurate, its material compliance might deviate from the target values due to fabrication constraints. A recent review highlighted that while many vascular models achieve excellent anatomical fidelity, few offer validated mechanical compliance close to human tissue. This gap means that the phantoms either end up too stiff or too distensible compared to an actual aorta, which in turn can lead to unrealistic hemodynamic behavior during experiments.

Another fundamental limitation is the absence of proper boundary conditions to mimic the *in vivo* environment. In a real human body, the aorta is surrounded by tissue and experiences external pressures (from the thoracic cavity, for instance) that influence its deformation. By contrast, an *in vitro* phantom placed in open air (or a simple water tank) with only internal pulsatile pressure can expand more freely than a real aorta would. Without an external chamber providing the correct counter-pressure or support, the phantom's behavior can be abnormal, exhibiting exaggerated radial expansion or compliance values outside the physiological range. In other words, a soft phantom pressurized in ambient conditions may not reproduce the same pressure–diameter relationship observed *in vivo*. This discrepancy impairs the fidelity of the model: pressure waveforms, flow patterns, and wall strain in the phantom can differ markedly from those in human arteries when

the phantom's compliance is not properly regulated. As a result, experiments conducted with an unconstrained phantom risk yielding data that do not translate well to real physiological conditions. This is a significant problem for in vitro cardiovascular studies and device testing, as the relevance of their findings hinges on how closely the model imitates the living system. In summary, the lack of a mechanism to control or tune the phantom's compliance in existing setups means that current in vitro models often fail to replicate true aortic behavior, motivating the need for a new solution[49].

### 1.3. Research Objectives

Accurate replication of physiological aortic behavior is essential for experimental cardiovascular modeling. In light of the limitations outlined above, this thesis aims to develop and characterize a compliance-controlled chamber system that enables an aorta phantom to exhibit in vivo-like compliance under dynamic pressure conditions. The specific research objectives of this work are as follows:

- Analytical Modeling: Develop a theoretical framework of the aortic phantom's mechanics by deriving the governing equations for a thin-walled cylindrical vessel under combined internal and external pressure. This involves employing a hyperelastic constitutive model (specifically, a Mooney–Rivlin formulation) to describe the aortic wall behavior and obtaining closed-form stress–strain or pressure–diameter relationships for the phantom. These equations will form the basis for predicting how the phantom responds to different pressure conditions and for quantifying its compliance.
- Hyperelastic Solution and Compliance Calibration: Using the derived model, determine the phantom's compliance and distensibility across physiological pressure ranges, and identify how external pressure can be adjusted to achieve target in vivo compliance values. In practice, this means linking the internal pressure loading (e.g. 80–120 mmHg pulsatile cycle) with an appropriate external counter-pressure so that the phantom's distensibility matches published human aortic data.
- Chamber Design and Prototyping: Create a detailed CAD design of the compliance-controlled chamber and its ancillary components to physically implement the proposed solution. The chamber will be a closed container surrounding the aorta phantom, with a tunable air–water interface that applies a uniform external pressure on the phantom wall. The design process involves determining the chamber dimensions, materials, seals, and pressure regulation mechanism (such as adjustable water column height or air pressure) to achieve fine control of external pressure.

The objective is to fabricate a chamber that is easy to operate and allows real-time adjustment of compliance during pulsatile experiments. This includes designing inlet/outlet ports for the flowing fluid, pressure sensors, and safety features. The final deliverable is a working prototype chamber that, when tested, can demonstrate the ability to maintain the aorta phantom's compliance within the desired physiological range.

Through these objectives, the thesis combines theoretical modeling, numerical simulation, and practical engineering design to solve the stated problem. Ultimately, the outcome will be a validated system in which an aortic phantom, aided by the compliance-controlled chamber, mimics the nonlinear pressure–diameter behavior of the native aorta under laboratory conditions.

## 1.4. Thesis Structure

This document is organized into chapters that mirror the multidisciplinary approach of the project. Chapter 2 (Literature Review) provides background on aortic anatomy, physiology, and the concept of compliance and distensibility, as well as an overview of existing in vitro models and phantom fabrication techniques relevant to this work. This review establishes the context and underpins the necessity for the compliance-controlled chamber. Chapter 3 (Materials and Methods) then details the methodological framework: it describes the development of the hyperelastic model and governing equations, the implementation of the Windkessel-based circulatory loop model, and the engineering design process of the chamber. Chapter 4 (Results) presents the key findings of the thesis. This includes the analytical and simulation results for the phantom's compliance behavior under various conditions, the validation of the model against expected physiological metrics, and the finalized design of the compliance-controlled chamber. Finally, the Conclusion summarizes the contributions of the thesis, discusses the limitations of the current setup, and offers suggestions for future research directions. This structured approach ensures a logical progression from fundamental theory to practical implementation, reflecting how the challenge of replicating aortic compliance is addressed from multiple angles in this work.

# 2 | Literature Review

## 2.1. Aorta

Chapters are typically subdivided into sections and subsections, and, optionally, sub-subsections, paragraphs and subparagraphs. All can have a title, but only sections and subsections are numbered.

### 2.1.1. Anatomy of the Aorta

The aorta, often referred to as the "greatest artery," is the primary conduit for distributing oxygenated blood from the heart to the entire systemic circulation. This large conductance blood vessel typically measures around 70 cm in length and 3.5 cm in diameter in adults. It originates from the left ventricle of the heart, extends inferiorly through the thorax and abdomen, and ultimately bifurcates into the two common iliac arteries [19].

For descriptive purposes, the aorta can be broadly categorized into two main sections based on anatomical compartment:

- **Thoracic Aorta:** This segment extends from the heart to the diaphragm.
- **Abdominal Aorta:** This portion continues from the diaphragm down to the aortic bifurcation.

A more detailed anatomical classification, often used in clinical and research settings, divides the aorta into five distinct sections [36]:

1. The Aortic Root
2. The Ascending Aorta
3. The Aortic Arch
4. The Isthmus and Descending Thoracic Aorta
5. The Abdominal Aorta

## The Aortic Root

The aortic root is a highly intricate and sophisticated structure that establishes the connection between the left ventricle of the heart and the systemic circulation. Its anatomical complexity has fascinated researchers for centuries, with early detailed descriptions and drawings attributed to Leonardo da Vinci in 1513 [10].

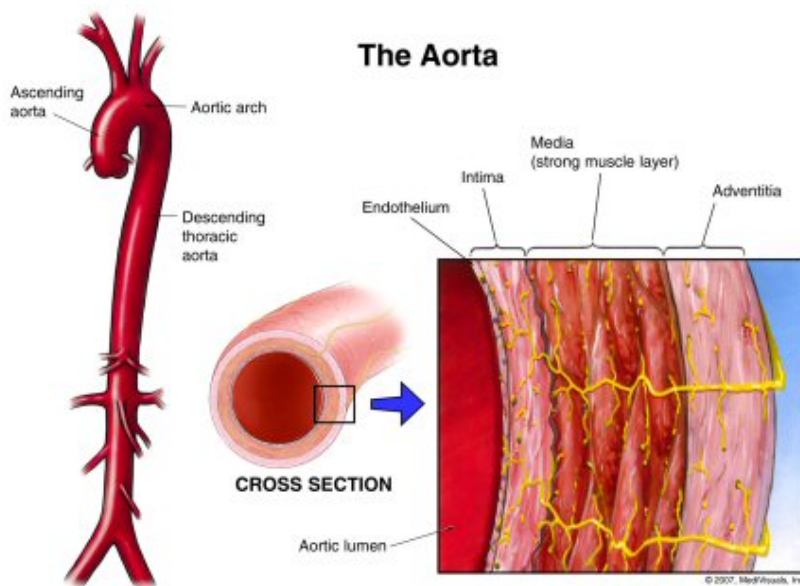


**Figure 2.1: Anatomical structure of the aorta**, including the ascending aorta, aortic arch, descending thoracic aorta, and vessel wall layers (intima, media, and adventitia)[9].

The aortic root is not a singular entity but rather an ensemble of interconnected components essential for proper cardiac function. These components include the aortic valve leaflets, their attachment points, the sinuses of Valsalva, the interleaflet trigones, the sinotubular junction, and the aortic annulus [47]. Despite extensive research, a universal consensus on the definitive description of aortic root anatomy remains elusive. The ventricular-aortic junction, for instance, can be conceptualized as both an anatomical interface between ventricular structures and aortic valvular sinuses, and a hemodynamic interface between ventricular structures and the semilunar lines of attachment of the arterial valvular leaflets [8]. Conventionally, the annulus is described as a virtual ring formed by connecting the basal attachment points of the leaflets within the left ventricle.

The coordinated dynamic behavior of all aortic root components is critical for optimal blood flow characteristics, efficient coronary perfusion, and proper left ventricular function

[47]. During ventricular systole, when the pressure generated by the left ventricle surpasses that in the ascending aorta, the aortic valve leaflets open. Conversely, as left ventricular pressure drops below aortic pressure, the leaflets close. The aortic valves are crucial for ensuring unidirectional blood flow without regurgitation, opening and closing millions of times annually over a lifetime. The primary structural component of valve cusps is collagen, constituting 43% to 55%, with elastin making up approximately 11% [36]. The composition and architecture of the valvular extracellular matrix (ECM) are fundamental to both their cyclical mechanical function and long-term durability.

Of particular physiological importance are the sinuses of Valsalva, which play two critical roles in aortic valve function [8]. Firstly, they provide essential space behind the open aortic leaflets, preventing occlusion of the coronary artery orifices. Secondly, this space facilitates the formation of eddy currents behind the leaflets when they are open, which contributes to valve closure and efficient blood flow dynamics.

## The Ascending Aorta

The ascending aorta is the segment of the aorta that extends from the aortic root to the origin of the brachiocephalic artery, which is the first great vessel branching from the aortic arch. Its typical length is approximately 5 cm, and its diameter can reach up to 2.6 cm, with variations influenced by individual body size. This segment is particularly susceptible to pathological conditions such as dissections and aneurysms [19].

## The Aortic Arch

The aortic arch is the curvilinear section of the aorta that extends from the origin of the brachiocephalic artery to the ostium of the left subclavian artery [36]. Its normal diameter is around 2.5 cm. The arch anatomically courses over the right pulmonary artery, the left mainstem bronchus, the left recurrent laryngeal nerve, and the roof of the left atrium. The primary branch vessels originating from the aortic arch include the brachiocephalic artery (which further divides into the right common carotid and right subclavian arteries), the left common carotid artery, and the left subclavian artery.

## The Isthmus and Descending Thoracic Aorta

The isthmus represents the narrowest portion of the aorta, measuring approximately 3 mm in diameter. It is located between the left subclavian artery and the ligamentum arteriosum, a fibrous remnant of the ductus arteriosus. In the fetal circulation, the ductus

arteriosus is a vital short conduit that allows blood to bypass the non-ventilated lungs. Postnatally, with falling prostaglandin concentrations and changing cardiac chamber pressures, the ductus arteriosus closes. The muscular walls of the ductus contract, directing blood from the pulmonary trunk into the newly ventilated lungs [47].

The descending thoracic aorta begins immediately distal to the isthmus and continues inferiorly to the level of the diaphragm. The esophagus typically runs alongside the descending aorta. The normal diameter of the proximal descending thoracic aorta is approximately 3.0 cm, gradually decreasing to less than 2.3 cm at the eleventh rib level. Branch vessels of the descending thoracic aorta include intercostal arteries, spinal arteries, and bronchial arteries.

## The Abdominal Aorta

The abdominal aorta commences at the hiatus of the diaphragm and courses retroperitoneally within the abdominal cavity until its bifurcation into the common iliac arteries. The normal diameter of the suprarenal abdominal aorta is approximately 2.0 cm, while the infrarenal abdominal aorta typically has a diameter equal to or less than 2.0 cm. Significant branch vessels of the abdominal aorta include the inferior phrenic arteries, celiac artery branches (supplying the liver, stomach, and spleen), renal arteries, superior mesenteric artery, inferior mesenteric artery, lumbar arteries, spinal arteries, and finally, the terminal common iliac arteries [19].

## The Intima

The intima is the innermost layer of the arterial wall, typically thin, ranging from approximately 0.05 to 0.1 mm in thickness. It is primarily composed of a single layer of \*\*endothelial cells\*\* that directly line the lumen, resting upon a thin \*\*basal lamina\*\*. Beneath the endothelium lies the \*\*subendothelial layer\*\*, which varies significantly in thickness depending on age and the presence of disease. This subendothelial layer is crucial for the load-carrying capacity of the wall and can range from almost imperceptible to geometrically dominant. It is predominantly made of \*\*collagen fibers\*\*, which exhibit a distinctive multi-layered organization but lack a uniform orientation throughout the layer's thickness. In pathological conditions such as \*\*atherosclerosis\*\*, the intima commonly thickens and stiffens due to the deposition of fatty substances, calcium, collagen fibers, cellular waste products, and fibrin [19].

## The Media

The media is the thick, middle layer of the aorta, with a typical thickness ranging from 0.1 to 0.5 mm. It represents the primary load-bearing component in the circumferential direction. This layer consists of a complex, three-dimensional network of \*\*smooth muscle cells, elastin, and bundles of collagen fibrils [8]. The media is distinctly separated from the intima by the internal elastic lamina and from the adventitia by the external elastic lamina.

Elastin, collagen bundles, and smooth muscle cells, along with their intricate interconnections, form a continuous fibrous helix within the media. This helix possesses a small pitch, resulting in a predominantly circumferentially oriented arrangement of fibers. This structured organization endows the media with its remarkable ability to withstand the high circumferential stresses exerted by blood pressure. Studies suggest that the distribution of collagen within the media does not appear to undergo significant changes in atherosclerotic arteries, unlike the intima [47].

## The Adventitia

The adventitia is the outermost layer of the arterial wall. It is generally thinner than the media, typically measuring between 0.25 and 0.40 mm in thickness. This layer is primarily composed of fibroblasts, fibrocytes, and thick bundles of collagen fibers [36]. The collagen within the adventitia is organized into two distinct helically arranged families of fibers.

The adventitia is enveloped by loose connective tissue, and its outer boundary is often not sharply defined, blending with the surrounding perivascular tissues. Its thickness can vary considerably, depending on the specific physiological function of the blood vessel. Similar to the media, the distribution of collagen in the adventitia does not show significant differences between normal and atherosclerotic arteries, suggesting its relative stability in the face of this disease process [19].

### 2.1.2. Pathology

#### Aortic stiffening

Aortic stiffening arises primarily from structural remodeling of the arterial wall, including elastin fragmentation, collagen deposition, and medial calcification. These changes diminish arterial compliance and accelerate pulse wave reflection, resulting in elevated systolic pressure, reduced diastolic pressure, and widened pulse pressure. The hemodynamic

consequences include increased left ventricular afterload, ventricular hypertrophy, and impaired coronary perfusion. Moreover, aortic stiffness is strongly correlated with hypertension and cardiovascular morbidity, contributing to microvascular injury in organs such as the brain and kidneys through elevated pulsatile energy transmission and endothelial dysfunction . Pulse wave velocity (PWV), which increases significantly with age and elastic fiber degradation, serves as the gold-standard metric for quantifying aortic stiffness . Therapeutic strategies targeting vascular aging—such as antihypertensives, lipid-lowering agents, and structured exercise—have demonstrated modest efficacy in mitigating arterial stiffening and preserving vascular function[29].

## Aortic Aneurysm

An aortic aneurysm is defined as a permanent, localized dilation of the aorta exceeding 50% of its normal diameter. These can occur throughout the aorta—including the ascending segment, arch, descending thoracic, and most commonly the infrarenal abdominal region. They typically arise from progressive degeneration of the aortic wall, characterized by elastic fiber fragmentation, smooth muscle loss, and collagen deposition.

Although the aneurysmal segment may exhibit increased local compliance, the structural integrity of the wall is compromised. According to Laplace's law ( $\sigma = \frac{P \cdot r}{2t}$ ), wall tension increases with radius, making large aneurysms particularly susceptible to rupture. Clinically, aneurysms are often silent until expansion or rupture. Thoracic aneurysms may present with chest or back pain or compress adjacent structures (e.g., hoarseness via recurrent laryngeal nerve involvement). Abdominal aortic aneurysms (AAAs) may manifest as pulsatile masses or, when ruptured, cause acute pain, hypotension, and often death.

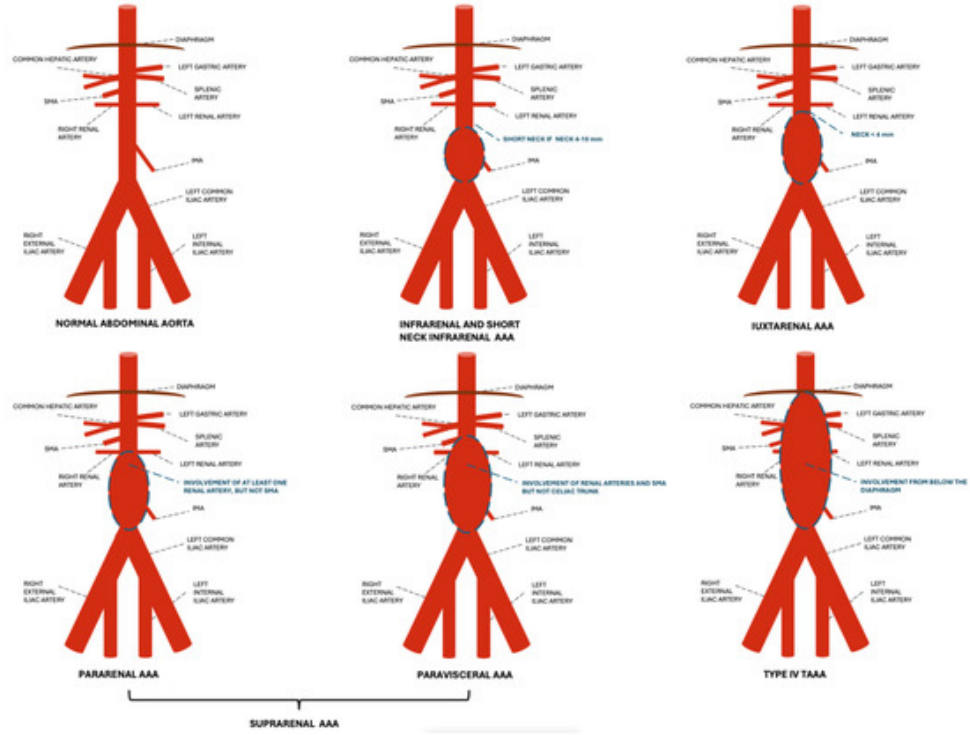


Figure 2.2: Classification of abdominal aortic aneurysms (AAAs) by location. (1) *Normal aorta*, (2) *Infrarenal* (3) *Short-neck infrarenal* (4) *Juxtarenal* (5) *Pararenal* (involves renal arteries), (6) *Paravisceral* (involves renal arteries and SMA) [34].

Imaging often reveals mural thrombus and calcification. Management depends on aneurysm size, growth rate, and symptoms. Surveillance is recommended for AAAs  $<5.0\text{--}5.5$  cm, while larger, symptomatic, or rapidly expanding aneurysms ( $>5$  mm in 6 months) warrant repair. Options include open surgical grafting or endovascular aneurysm repair (EVAR). Notably, EVAR introduces a stiff endograft that reduces aortic compliance and increases pulse wave velocity, potentially contributing to left ventricular hypertrophy and increased cardiac afterload. Adjunctive therapies focus on lowering wall stress (e.g., antihypertensives) and mitigating risk factors to limit aneurysm progression.[12][4]

## Aortic Dissection

An aortic dissection is a life-threatening condition characterized by a tear in the innermost layer of the aorta (the intima), allowing blood to penetrate into the medial layer and create a false lumen. This disrupts normal flow and can compromise perfusion to vital organs by compressing the true lumen or occluding branch vessels.

Dissections are classified based on their anatomical location using the Stanford system:

Type A involves the ascending aorta, often extending from the aortic root or arch.

Type B is confined to the descending aorta, with the tear originating distal to the left subclavian artery.

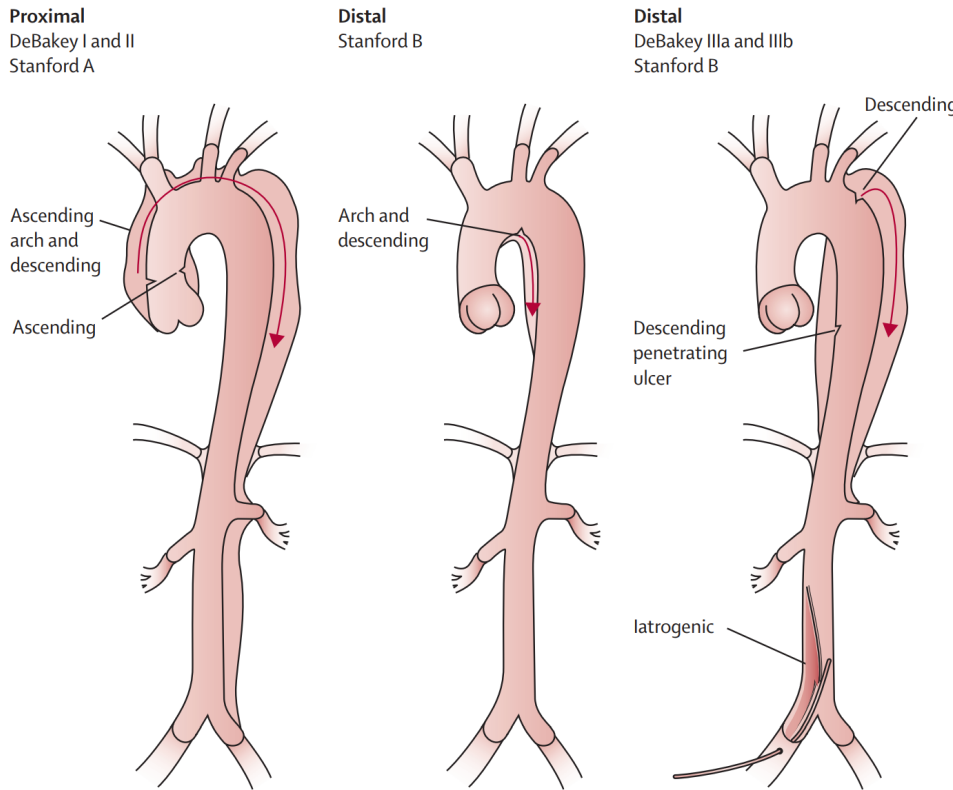


Figure 2.3: Anatomical classification of aortic dissection based on the DeBakey and Stanford systems. Adapted from Nienaber and Clough [28].

Type A dissections are more dangerous, as they can rapidly lead to hemodynamic collapse due to cardiac tamponade, acute aortic regurgitation, or rupture. Clinical signs may include chest pain, a widened mediastinum on imaging, unequal blood pressures between arms, or a new diastolic murmur. Urgent surgical repair (typically replacement of the ascending aorta) is required to prevent death.

Type B dissections, involving only the descending aorta, are often managed medically with aggressive blood pressure and heart rate control using intravenous  $\beta$ -blockers and vasodilators to reduce shear stress. However, intervention (such as endovascular stent-graft placement) becomes necessary in cases of complications like organ malperfusion, aneurysmal expansion, or impending rupture.

Across both types, the dissection acutely impairs aortic compliance and disrupts normal

hemodynamics. Long-term management includes serial imaging to monitor for aneurysm formation or dissection extension, along with strict control of hypertension to reduce the risk of recurrence.

## 2.2. Compliance and distensibility

### 2.2.1. Compliance and its role in cardiovascular modeling

The aorta, besides being the main vessel to distribute blood to the arterial system, dampens the pulsatile pressure that results from the intermittent outflow from the left ventricle. The actual dampening is a function of aortic compliance. Large arteries branching off the aorta (e.g., carotid, mesenteric, renal arteries) distribute the blood flow to specific organs. These large arteries, although capable of constricting and dilating, play only a small role in regulating pressure and blood flow under normal physiological conditions. Once a large artery reaches the organ it supplies, it branches into small arteries that distribute blood flow within the organ.

These vessels continue to branch and become smaller arterioles. Together, the small arteries and arterioles represent the primary vessels that are involved in regulating arterial blood pressure and blood flow within the organ. These vessels are highly innervated by autonomic nerves (particularly sympathetic adrenergic), and respond to changes in nerve activity and circulating hormones by constricting or dilating. Therefore, these vessels are referred to as resistance vessels. As arterioles approach 10 microns in diameter, they lose their smooth muscle to become capillaries, and comprise endothelial cells and a basement membrane. Capillaries represent the smallest vessels within the microcirculation and are the primary exchange vessels within the body. [20]

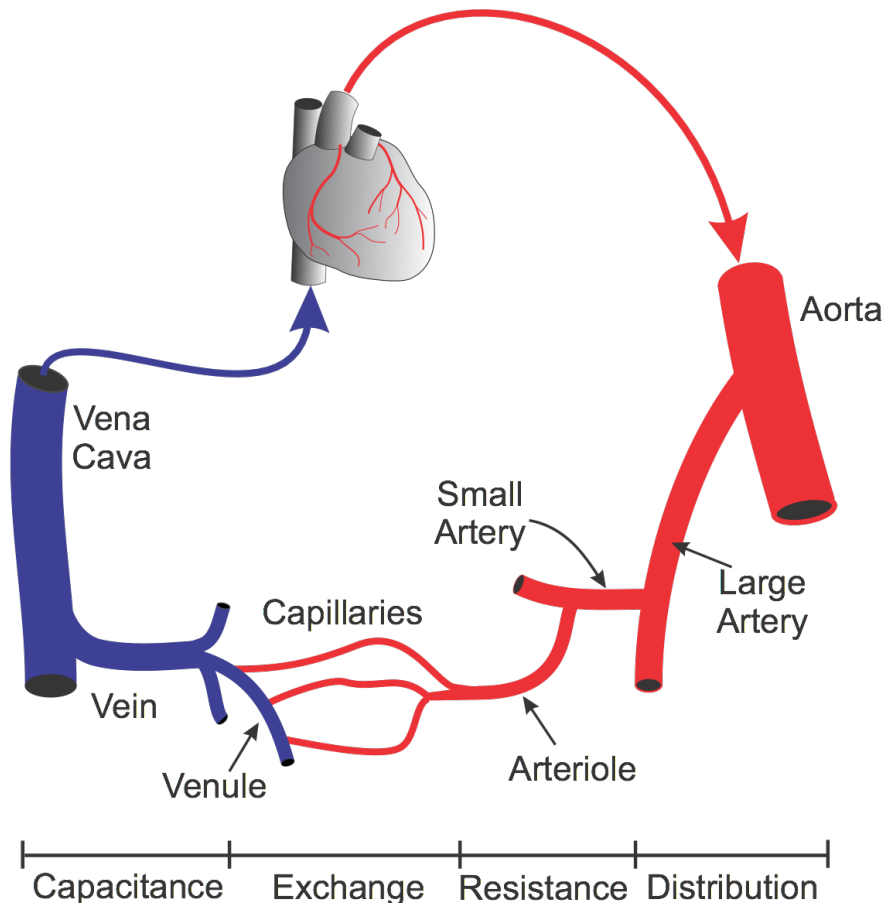


Figure 2.4: functions of different blood vessels [20]

The physiological significance of aortic compliance is paramount in understanding the intricate dynamics of the cardiovascular system. The compliance of an artery refers to its inherent ability to distend and expand with an increase in internal pressure. In the largest artery, the aorta, high compliance during the systolic phase of the cardiac cycle is crucial. This allows the vessel to efficiently expand and temporarily store a significant volume of ejected blood. This stored volume is then gradually released during diastole, the relaxation phase of the heart, thereby maintaining a more continuous and less pulsatile blood flow to the peripheral circulation. This remarkable buffering action is widely known as the Windkessel effect, and it serves to effectively moderate pulse pressure fluctuations and concurrently reduce the workload imposed on the left ventricle. Conversely, a reduction in aortic compliance, commonly observed as a natural consequence of aging or as a pathological manifestation in various cardiovascular diseases, leads to a stiffer aorta. This increased stiffness results in a higher systolic pressure, a widened pulse pressure, and a subsequent increase in cardiac strain due to the heart having to pump against a less distensible system. Clinically, measuring aortic compliance provides invaluable insights into

overall vascular health; for instance, a markedly decreased compliance is a significant indicator associated with conditions such as hypertension and generalized arteriosclerosis[27].

### 2.2.2. state of art

The fundamental definition of compliance ( $C$ ) in arterial mechanics is the change in volume ( $\Delta V$ ) corresponding to a given change in internal pressure ( $\Delta P$ ). This relationship is expressed as:

$$C = \frac{\Delta V}{\Delta P} \quad (2.1)$$

This equation represents a core hemodynamic quantity, with conventional units of volume per pressure, such as milliliters per millimeter of mercury (mL/mmHg). A high value for compliance indicates a vessel that undergoes a large volume change for a relatively small pressure change, signifying a highly distensible vessel. Conversely, a low compliance value is characteristic of a stiff or rigid vessel. Within the healthy adult arterial system, the total arterial compliance is typically on the order of a few mL/mmHg. For illustrative purposes, a representative value might be approximately 2 mL/mmHg. This specific compliance value would correspond to a normal pulse pressure of approximately 40 mmHg for a typical stroke volume of around 80 mL. Conceptually, compliance can be visualized as the slope of the volume-pressure curve for an artery. It is important to note that for arteries, this slope is not constant; rather, it typically decreases at higher pressures, reflecting the non-linear stiffening behavior of the arterial wall tissues as they are stretched further[17].

For a simplified cylindrical vessel, such as an idealized arterial segment of length  $L$  and internal radius  $R$  (where the diameter  $D = 2R$ ), the volume can be expressed as  $V = \pi R^2 L$ . By applying differentiation,  $dV/dR = 2\pi R L$ . Using the chain rule, the compliance can be elegantly written as:

$$C = \frac{dV}{dP} = \frac{dV}{dR} \frac{dR}{dP} = 2\pi R L \frac{dR}{dP} \quad (2.2)$$

This expression inherently relates the change in radius ( $dR/dP$ ) induced by a pressure change to the resultant volume change[44]. To further develop this relationship, one must incorporate the mechanical properties of the vessel wall, specifically how its radius changes in response to pressure. In the context of the linear elastic regime, applicable for small deformations, the hoop (circumferential) strain( $\lambda_\theta$ ) is defined as the fractional change in diameter:

$$\lambda_\theta \approx \frac{\Delta D}{D_0} = \frac{\Delta R}{R_0} \quad (2.3)$$

Here,  $D_0$  denotes the initial diameter, and  $R_0 = D_0/2$  is the initial radius. For a thin-

walled tube, Laplace's law provides the relationship for hoop stress ( $\sigma_\theta$ ) as  $\sigma_\theta \approx \frac{PR}{t}$  (or  $\sigma_\theta = \frac{PD}{2t}$ , where  $t$  is the wall thickness). Assuming the vessel wall exhibits linear elastic behavior with a Young's modulus  $E$  and is free to expand longitudinally (rendering axial stress negligible), Hooke's law states that the hoop strain is approximately related to hoop stress by  $\epsilon_\theta \approx \sigma_\theta/E$ . Combining these principles, an incremental pressure  $\Delta P$  is observed to produce an approximate change in diameter given by:

$$\frac{\Delta D}{D_0} \approx \frac{\Delta P}{E} \frac{D_0}{2t} \quad (2.4)$$

Rearranging this, we find:

$$\Delta D \approx \frac{\Delta P D_0^2}{2 E t} \quad (2.5)$$

This linear approximation clearly indicates that the change in diameter is directly proportional to the applied pressure change, with the proportionality constant involving the material stiffness ( $E$ ) and the vessel's initial geometry ( $D_0$ ,  $t$ ). Substituting the expression for  $\Delta R$  (which is  $\Delta D/2$ ) from Equation 2.5 into Equation 2.2 yields a particularly useful formula for the compliance of a cylindrical vessel expressed in terms of its baseline dimensions and fundamental material properties:

$$C \approx 2\pi R_0 L \left( \frac{\Delta R}{\Delta P} \right) \approx 2\pi R_0 L \left( \frac{R_0^2}{E t} \right) = \frac{2\pi R_0^3 L}{E t} \quad (2.6)$$

Rewriting this expression in terms of the initial diameter  $D_0 = 2R_0$ , we obtain:

$$C \approx \frac{\pi L D_0^3}{4 E t} \quad (2.7)$$

This result elegantly highlights that compliance exhibits a strong cubic dependence on the baseline diameter ( $\propto D_0^3$ ) and is inversely proportional to both the wall stiffness (Young's modulus  $E$ ) and the wall thickness ( $t$ ). Consequently, a large, thin-walled, and highly elastic tube will possess very high compliance, whereas a small, thick, or inherently stiff tube will demonstrate low compliance[15]. It is crucial to acknowledge that in physiological reality, arterial walls are complex, anisotropic, and exhibit nonlinear mechanical behavior. Therefore, compliance diminishes significantly at higher pressures as the less extensible collagen fibers within the wall become increasingly engaged, and the linear formulas presented above are strictly applicable only within the low-strain elastic regime.

## Distensibility

While compliance ( $C$ ) is an absolute measure that depends directly on the physical size of a vessel, distensibility serves as a normalized metric of the vessel's elasticity, designed to be independent of its absolute dimensions. Distensibility is characteristically defined as the fractional (or relative) change in a specific dimension (e.g., diameter or area) per unit change in pressure. For instance, in terms of diameter, diametric distensibility ( $D_d$ ) can be formally defined as:

$$D_d = \frac{\Delta D/D_0}{\Delta P} \quad (2.8)$$

This formulation yields units of  $\text{mmHg}^{-1}$  (as  $\Delta D/D_0$  is dimensionless). Diametric distensibility represents the relative change in the vessel's diameter for a given increment in pressure. Alternatively, if cross-sectional area ( $A$ ) is utilized, the areal distensibility ( $D_A$ ) is defined as  $D_A = \frac{\Delta A/A_0}{\Delta P}$ . Similarly, a volumetric distensibility could be defined as  $\Delta V/V_0$  per  $\Delta P$ . All these definitions of distensibility are interrelated; for instance, for small strains,  $\Delta A/A_0 \approx 2\Delta D/D_0$ . It is therefore paramount in any hemodynamic study to explicitly specify which definition of distensibility (e.g., diametric, areal, or volumetric) and corresponding units are being employed. In many hemodynamic and imaging-based studies, distensibility is frequently reported based on changes in cross-sectional area as measured by modalities like Magnetic Resonance Imaging (MRI) or echocardiography. Conversely, in theoretical modeling or bench-top experiments, the choice between volume or diameter may depend on the specific parameter being measured[33][39].

Using the diameter-based definition (Equation 2.8), a distensibility value on the order of  $10^{-3} \text{ mmHg}^{-1}$  is typically considered normal for large arteries. In the ascending aorta of a healthy young adult, reported distensibility values are often considerably higher, frequently falling within the range of  $5-9 \times 10^{-3} \text{ mmHg}^{-1}$ . Notably, these values are observed to decline progressively with increasing age[32]. In older individuals or those with pathologically stiffer aortas, diametric distensibility may decrease significantly, falling to approximately  $2 \times 10^{-3} \text{ mmHg}^{-1}$  or even lower. Thus, a generally accepted physiological range for aortic distensibility in middle-aged adults typically spans approximately  $2-4 \times 10^{-3} \text{ mmHg}^{-1}$ , with younger, healthier aortas often exhibiting values at the upper end of this range or even exceeding it, while diseased or elderly aortas fall towards the lower end.

The human thoracic aorta is not a homogenous structure in terms of its elastic properties, exhibiting significant regional variations in distensibility. The more proximal segments, specifically the ascending aorta and the aortic arch, are generally more distensible than the more distal segments, such as the descending aorta. This difference is largely attributable

to variations in their extracellular matrix composition, with proximal segments containing a higher proportion of elastic fibers. Table 2.1 summarizes representative literature values of area distensibility (fractional cross-sectional area change per pressure) across different aortic regions in healthy subjects. These types of measurements are commonly obtained via advanced imaging techniques such as MRI from cohorts spanning various age groups, often reported as mean  $\pm$  standard deviation. As generally anticipated, the ascending aorta consistently presents as the most distensible segment on average, with a gradual, albeit slight, decrease in distensibility observed as one moves distally along the aorta. (It is important to note that the distensibility values presented here are in units of  $10^{-3}$  mmHg $^{-1}$ ; for instance, a value of 8.9 in the table corresponds to  $8.9 \times 10^{-3}$  mmHg $^{-1}$ ). With increasing age, it is universally observed that all of these regional distensibility values would predictably decrease as the aortic wall undergoes further stiffening[13].

In reporting distensibility, some studies may specifically use the term "distensibility coefficient" to refer to the area-based metric. It is paramount to always clarify the precise definition of distensibility being employed, as variations exist. Volumetric distensibility (or compliance), often expressed in units like mL/mmHg or normalized as % per mmHg, is frequently used when considering the entire arterial tree or the total volume change of a larger vessel segment. In contrast, cross-sectional distensibility (either areal or diametric) is commonly employed for assessing local elasticity measured via advanced imaging techniques. The cross-sectional measurement methods typically assume that the longitudinal length of the arterial segment does not change significantly with pressure variations, implying that the observed area change effectively captures the volumetric change of that specific segment (i.e.,  $\Delta V \approx L \cdot \Delta A$  for a segment of fixed length  $L$ ). Conversely, when employing ultrasound to examine a superficial artery, clinicians often directly measure diameter changes, leading to a diametric distensibility. For small strains, this diametric distensibility will be approximately half of the areal distensibility, given that  $\Delta A/A_0 \approx 2\Delta D/D_0$ . All these forms of distensibility are valid and interrelated, with the specific choice often dictated by the chosen measurement technique. In summary, for meaningful comparisons, literature values of distensibility should only be contrasted if they are based on the identical definition (e.g., area-based vs. diameter-based) and share consistent units.

**Table 2.1: Representative Aortic Distensibility Values ( $\times 10^{-3}\text{mmHg}^{-1}$ ) by Aortic Segment and Sex in Healthy Subjects[42].**

Aortic Segment	Male Mean $\pm$ SD	Female Mean $\pm$ SD	Total Mean $\pm$ SD
Ascending Aorta	8.5 $\pm$ 4.2	9.2 $\pm$ 3.0	8.9 $\pm$ 3.6
Aortic Arch	7.2 $\pm$ 3.4	8.0 $\pm$ 3.3	7.7 $\pm$ 3.3
Aortic Isthmus	7.0 $\pm$ 2.7	7.7 $\pm$ 2.3	7.4 $\pm$ 2.5
Descending Aorta	7.7 $\pm$ 2.7	8.8 $\pm$ 3.1	7.7 $\pm$ 3.0

The values presented in Table 2.1 illustrate both the intrinsic regional differences in aortic elasticity and the considerable variability observed among individuals, as evidenced by the sizable standard deviations. For instance, in this young cohort, the ascending aorta's distensibility averages around  $9 \times 10^{-3} \text{ mmHg}^{-1}$ , while the more distal descending aorta exhibits a lower value, typically around  $7 \times 10^{-3} \text{ mmHg}^{-1}$ . As individuals age, it is consistently observed that all these regional distensibility values predictably decrease, correlating with the progressive stiffening of the aortic wall.

The precise measurement of aortic distensibility holds significant clinical utility. It plays a pivotal role in the early detection of vascular aging and the onset of arterial disease, facilitates the stratification of cardiovascular risk in various patient populations, and ultimately guides the development of personalized treatment strategies, particularly for managing conditions such as hypertension, diabetes, and aortic aneurysms.



# 3 | Materials and Methods

## 3.1. Overall workflow

In this work, we propose a comprehensive design and modeling pipeline aimed at tuning the compliance of a patient-specific aortic phantom through external pressure control. The objective is to mimic physiological aortic behavior by leveraging both theoretical modeling and practical engineering approaches. The overall methodology is outlined as follows.

First, the geometry of the aorta was extracted from a computed tomography (CT) scan of a patient diagnosed with abdominal aortic aneurysm (AAA) and scheduled for surgical intervention. The segmentation process involved isolating the aortic lumen and refining the mesh to ensure smooth surfaces suitable for further modeling. To simplify the geometry while retaining physiological relevance, the three upper branches of the aortic arch (brachiocephalic, left common carotid, and left subclavian arteries) were excluded. The final STL model included the ascending aorta, aortic arch, descending thoracic and abdominal aorta, and the bifurcation into the two iliac arteries.

The STL file was then imported into Fusion 360, where the mesh was reduced and converted into a solid body to facilitate design operations. Based on this anatomical geometry, a hyperelastic constitutive model was employed to describe the mechanical behavior of the aortic wall. Specifically, the Mooney–Rivlin strain energy function was adopted and integrated with thin-wall assumptions to derive a pressure–diameter relationship. This coupling provided the theoretical foundation for compliance estimation.

To regulate the compliance of the phantom, we designed a pressure-controlled closed chamber that applies uniform external pressure through a water–air interface. A parametric equation was implemented in MATLAB to link the internal aortic pressure (ranging from 80 to 120 mmHg) and the external water column height (1–20 cm) to the resulting strain in the phantom wall. This model allowed the identification of optimal water levels required to reproduce physiological compliance values reported in the literature.

Following this, a lumped parameter model (LPM) was developed to simulate the hemodynamic behavior of the phantom in steady-state conditions. This step was essential to ensure that the pressure drop and resistance of the phantom were consistent with physiological expectations. The hydraulic resistance of the system was roughly estimated and validated against values from existing studies.

Finally, the design of the compliance chamber and associated components (e.g., lid, clamps, inlet/outlet ports) was performed in Fusion 360. The detailed mechanical design and fabrication considerations are provided in the following subsections and further elaborated in the Results section.

## 3.2. Mathematical modelling

### 3.2.1. Constitutive Equation

This document presents the detailed derivation of the Cauchy stress tensor for an incompressible, isotropic, hyperelastic cylindrical tube using the Mooney-Rivlin strain energy function.

Let  $\mathbf{F}$  denote the deformation gradient tensor.

Right Cauchy-Green Deformation Tensor

$$\mathbf{C} = \mathbf{F}^T \mathbf{F}$$

**Left Cauchy-Green Deformation Tensor**

$$\mathbf{B} = \mathbf{F} \mathbf{F}^T$$

**Strain Invariants**

$$I_1 = \text{tr}(\mathbf{C})$$

$$I_2 = \frac{1}{2} [(\text{tr}(\mathbf{C}))^2 - \text{tr}(\mathbf{C}^2)]$$

$$I_3 = \det(\mathbf{C})$$

For incompressible materials:

$$I_3 = \det(\mathbf{C}) = 1$$

3. Strain Energy Function (SEF) Assuming an isotropic, hyperelastic material, the strain energy density function  $W$  depends on the invariants:

$$W = W(I_1, I_2)$$

4. Cauchy Stress Tensor The general form of the Cauchy stress tensor for an incompressible isotropic hyperelastic material is:

$$\boldsymbol{\sigma}_{\text{iso}} = 2 \left[ \frac{\partial W}{\partial I_1} \mathbf{B} + \frac{\partial W}{\partial I_2} (I_1 \mathbf{I} - \mathbf{B}) \right] - p \mathbf{I}$$

Where:

- $p$  is a Lagrange multiplier enforcing incompressibility,
- $\mathbf{I}$  is the identity tensor.

5. Mooney-Rivlin Model In the Mooney-Rivlin model, the SEF is:

$$W = C_1(I_1 - 3) + C_2(I_2 - 3)$$

Therefore,

$$\begin{aligned} \frac{\partial W}{\partial I_1} &= C_1 \\ \frac{\partial W}{\partial I_2} &= C_2 \end{aligned}$$

and their Derivative with respect to  $C$ :

$$\begin{aligned} \frac{\partial I_1}{\partial C} &= I \\ \frac{\partial I_2}{\partial C} &= I_1 I - C^T \end{aligned}$$

Considering Incomperssibility, we will have:

$$\boldsymbol{\sigma}_{\text{iso}} = 2 * (C_1 \mathbf{B} - C_2 (\mathbf{B}^{-1} \mathbf{I})) - p \mathbf{I}$$

where  $\mathbf{B}$  is the left Cauchy-Green deformation tensor, defined as:

$$\mathbf{B} = \begin{bmatrix} \lambda_r^2 & 0 & 0 \\ 0 & \lambda_\theta^2 & 0 \\ 0 & 0 & \lambda_z^2 \end{bmatrix}$$

6. Axisymmetric Deformation Assumptions for Cylinder Assume a cylindrical tube with principal stretches:

$$\lambda_r, \lambda_\theta, \lambda_z$$

Due to incompressibility:

$$\lambda_r \lambda_\theta \lambda_z = 1$$

And we have a constraint in two ending of the pipe, meaning, we do not have any changes in lenght of the phantom. Therefore we will have:

$$\lambda_r = \frac{t}{t_0}, \quad \lambda_\theta = \frac{D}{D_0}, \quad \lambda_z = 1 \Rightarrow \lambda_r = \frac{1}{\lambda_\theta}$$

Where  $t$  is thickness and  $D$  is diameter of tube.

7. Deformation Tensors in Matrix Form

$$\mathbf{B} = \begin{bmatrix} \lambda_\theta^{-2} & 0 & 0 \\ 0 & \lambda_\theta^2 & 0 \\ 0 & 0 & 1 \end{bmatrix}$$

8. Final Component Form of Stress

$$\begin{aligned} \sigma_{rr} &= 2(C_1 \lambda_\theta^{-2} - C_2 \lambda_\theta^2) - p \\ \sigma_{\theta\theta} &= 2(C_1 \lambda_\theta^2 - C_2 \lambda_\theta^{-2}) - p \\ \sigma_{zz} &= 2(C_1 - C_2) - p \end{aligned}$$

Considering thin-wall assumptions for cylindrical structures, the ratio of the wall thickness  $t$  to the diameter  $D$  must typically satisfy the condition  $\frac{t}{D} < 0.1$  [? ]. Given that our tube has a thickness of  $t = 2$  mm and a diameter of  $D = 20$  mm, the calculated ratio is:

$$\frac{t}{D} = \frac{2}{20} = 0.1$$

This places our structure precisely at the conventional boundary limit of thin-wall theory. Despite this marginal condition, we can reasonably employ the thin-wall assumption for analytical simplifications.

Under the thin-wall condition, the radial stress component is assumed negligible:

$$\sigma_{rr} \approx 0$$

Applying this condition and substituting the resulting expression for the Lagrange multi-

plier (pressure)  $p$  into the circumferential stress equation derived from the Mooney-Rivlin material model, we obtain:

$$\sigma_{\theta\theta} = 2(C_1 + C_2)(\lambda_\theta^2 - \lambda_\theta^{-2})$$

This final simplified expression for circumferential stress has been independently developed for the context of this study.

### 3.2.2. Thin-wall Hoop Stress for Cylindrical Tube

For a cylindrical tube experiencing internal pressure ( $P_{\text{in}}$ ) and external pressure ( $P_{\text{ext}}$ ), the hoop stress is also expressed by the classical thin-wall approximation:

$$\sigma_{\theta\theta} = \frac{(P_{\text{in}} - P_{\text{ext}})D}{2t} \quad (3.1)$$

Here,  $D$  represents the diameter of the tube, and  $t$  represents its thickness.

Equating these two expressions for the hoop stress gives:

$$2(C_1 + C_2)(\lambda_\theta^2 - \lambda_\theta^{-2}) = \frac{(P_{\text{in}} - P_{\text{ext}})D}{2t} \quad (3.2)$$

Now, considering the geometric relationships of deformation, we define:

$$\lambda_\theta = \frac{D}{D_0} \rightarrow D = D_0\lambda_\theta \quad (3.3)$$

$$\lambda_r = \frac{t}{t_0} \rightarrow t = \frac{t_0}{\lambda_\theta} \quad (3.4)$$

Substituting these relationships back into the equation, we obtain a comprehensive formulation explicitly linking pressure conditions, geometric dimensions, and material parameters:

$$2(C_1 + C_2)(\lambda_\theta^2 - \lambda_\theta^{-2}) = \frac{(P_{\text{in}} - P_{\text{ext}})D_0\lambda_\theta^2}{2t_0} \quad (3.5)$$

This equation serves as a foundational basis for further analysis and the design of cylindrical tubes under internal and external pressure conditions.

### 3.2.3. Definition of Internal and External Pressure

In the experimental setup developed to replicate physiological aortic behavior, it is essential to define both the internal and external pressures applied to the compliant cylindrical phantom.

#### Internal Pressure $P_{\text{in}}$

The *internal pressure*, denoted as  $P_{\text{in}}$ , simulates the luminal blood pressure within the aorta. In our system, it is generated and controlled using a mechanical pump, and is maintained within a physiologically relevant range of 80–120 mmHg, corresponding to typical systolic and diastolic pressures observed in the human circulatory system.

#### External Pressure $P_{\text{ext}}$

The *external pressure*,  $P_{\text{ext}}$ , is a controlled design parameter applied to the outer surface of the phantom. This pressure is a combination of compressed air and hydrostatic water pressure within a sealed chamber. The objective is to regulate the transmural pressure and allow fine-tuning of the tube's compliance.

The total external pressure is given by:

$$P_{\text{ext}} = P_{\text{air}} + P_{\text{water}} = \frac{P_0 V_0}{V_0 - \Delta V} + \rho g h_{\text{water}} \quad (3.6)$$

where:

- $P_0$  is the initial air pressure,
- $V_0$  is the initial volume of air,
- $\Delta V$  is the change in volume due to displacement,
- $\rho$  is the density of water,
- $g$  is the gravitational acceleration,
- $h_{\text{water}}$  is the height of the water column above the tube.

This formulation permits experimental manipulation of  $P_{\text{ext}}$  through control of air compression and water level, allowing precise adjustment of boundary conditions.

#### Governing Equation for Pressure Balance

By coupling the external pressure formulation with the hyperelastic constitutive equation of the Mooney–Rivlin model and assuming a thin-walled cylindrical geometry, we derive the governing pressure balance as follows:

$$P_{\text{in}} - \left( \frac{P_0 V_0}{V_0 - \Delta V} + \rho g h \right) = \frac{4(C_1 + C_2)t_0}{\lambda_\theta^2 D_0} \left( \lambda_\theta^2 - \frac{1}{\lambda_\theta^2} \right) \quad (3.7)$$

## Volume Displacement Due to Phantom Expansion

The change in air volume  $\Delta V$  in the external chamber arises from the expansion of the compliant phantom as it deforms radially under internal pressure. This expansion displaces the surrounding air, thereby altering the external pressure according to Boyle's law.

Assuming the tube is constrained axially and only expands radially, the displaced volume can be expressed as:

$$\Delta V = \frac{\pi}{4} D_0^2 \lambda_\theta^2 (\lambda_\theta^2 - 1) \quad (3.8)$$

Here,  $\lambda_\theta = \frac{D}{D_0}$  is the circumferential stretch ratio,  $D_0$  is the initial diameter, and the term  $\lambda_\theta^2 - 1$  represents the relative expansion of the cross-sectional area.

Substituting Equation (3.8) into the expression for external pressure, and subsequently into the pressure balance equation, we obtain the final comprehensive relation governing the mechanical equilibrium of the system:

$$P_{\text{in}} - \left( \frac{P_0 V_0}{V_0 - \frac{\pi}{4} D_0^2 \lambda_\theta^2 (\lambda_\theta^2 - 1)} + \rho g h \right) = \frac{4(C_1 + C_2)t_0}{\lambda_\theta^2 D_0} \left( \lambda_\theta^2 - \frac{1}{\lambda_\theta^2} \right) \quad (3.9)$$

This equation fully characterizes the interplay between internal pressurization, externally regulated boundary conditions, and the nonlinear elastic response of the phantom. It forms the theoretical foundation for calibrating the compliance box and ensuring the physiological relevance of the mock circulatory system.

with:

- $C_1, C_2$  as Mooney–Rivlin material constants,
- $\lambda_\theta = \frac{D}{D_0}$  the circumferential stretch ratio,
- $t_0$  the initial wall thickness of the tube,

- $D_0$  the initial undeformed diameter.

Equation (3.7) serves as the fundamental relation for evaluating the mechanical response of the phantom under various loading conditions. It is used to design the compliant chamber and validate experimental pressure-deformation responses.

### 3.3. Modeling the Circulatory Loop Using a Windkessel Approach

Modern mock circulatory loops (MCLs) routinely employ Windkessel models to replicate the compliance of the aorta and the resistance of the peripheral vasculature [48]. The Windkessel concept, originally introduced by Otto Frank, treats the arterial system as a combination of resistive and compliant elements that buffer pulsatile flow. In an MCL, this is typically achieved with an *arterial compliance chamber* (often an air-filled chamber or elastic element) and an adjustable resistance valve to simulate total systemic vascular resistance [48]. The aortic compliance is essential for damping the pulsatile pressure fluctuations and maintaining diastolic flow, and thus a compliant chamber (a physical realization of a capacitor) is included to mimic the elastic storage of blood in the aorta [48]. The peripheral resistance, representing the systemic arteriolar resistance, is usually implemented by a pinch valve, needle valve, or adjustable clamp that creates a controlled pressure drop, analogous to a resistor in the circuit [48]. Together, these elements form a Windkessel that reproduces physiologic aortic pressure and flow waveforms *in vitro*.

The cardiovascular system can be effectively modeled using lumped parameter models (LPMs), also referred to as Windkessel models, which provide simplified yet accurate representations of complex arterial fluid dynamics. The foundational Windkessel models were initially proposed by Frank in 1899, representing systemic arterial compliance and peripheral resistance using an analogy to electrical circuits, comprising resistors and capacitors [21].

The simplest version, the 2-element Windkessel model (Figure 1a), describes arterial compliance ( $C$ ) and peripheral resistance ( $R$ ). Compliance represents the vessel wall elasticity, which stores blood during systole and releases it during diastole, analogous to an electrical capacitor. Peripheral resistance represents the frictional losses due to viscosity and vessel geometry, akin to an electrical resistor [21].

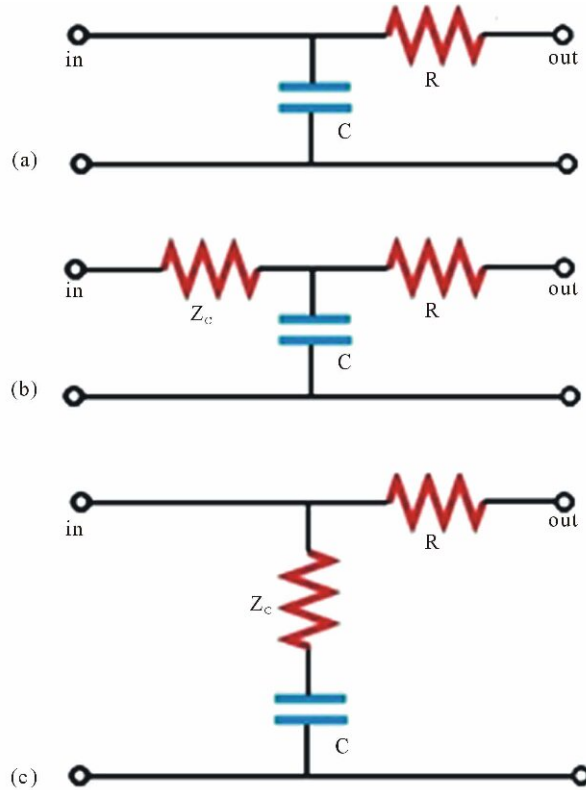


**Figure 3.1:** Windkessel models commonly used in lumped parameter cardiovascular simulations. (a) Two-element model consisting of a resistor and a capacitor. (b) Classical three-element Windkessel model introduced by Westerhof et al. with proximal impedance  $Z_c$ . (c) Modified 3-element configuration with  $Z_c$  in series[21].

However, this 2-element model was insufficient in describing the high-frequency oscillatory phenomena associated with pulse waves. Westerhof et al. expanded upon this by introducing the characteristic impedance element ( $Z_c$ ), forming the 3-element Windkessel model (Figure 1b). This impedance accounts for wave reflection phenomena, enhancing the accuracy of the model in simulating systolic pressures (Westerhof et al., 1969; [21]). Another variant by Buratini places  $Z_c$  in series with compliance (Figure 1c), emphasizing the elasto-viscous characteristics of arterial walls ([21]).

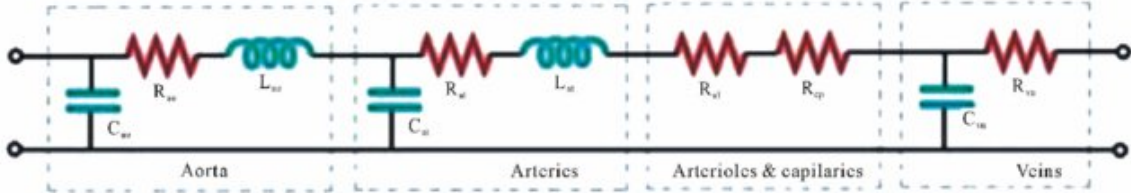


**Figure 3.2:** Example of a multi-compartment lumped parameter model representing the systemic circulation. The diagram includes the aorta ( $C_{ao}$ ,  $R_{ao}$ ,  $L_{ao}$ ), arteries, arterioles and capillaries, and veins, each represented by combinations of resistive ( $R$ ), capacitive ( $C$ ), and inertive ( $L$ ) elements[21].

To further improve modeling accuracy, particularly at lower frequencies, a fourth inertial element (L) was introduced, representing blood inertia (Figure 2). This 4-element Windkessel model provides a more detailed representation of the arterial system, explicitly capturing inertial effects of blood flow in larger arteries, such as the aorta ([21]).

The systemic circulation is often divided into multi-compartment models (Figure 2), each segment described by a combination of resistances (R), compliances (C), and inertances (L), tailored according to the local vascular properties. In particular, the aorta segment comprises compliance ( $C_{ao}$ ), viscous resistance ( $R_{ao}$ ), and inertance ( $L_{ao}$ ), collectively simulating physiological hemodynamics more precisely ([21]).

Thus, the Windkessel lumped parameter modeling approach, incorporating multiple elements, offers an efficient and accurate means to represent complex cardiovascular dynamics, particularly within the aortic segment. Such models are invaluable for understanding physiological and pathological conditions, aiding in diagnostics, therapeutic planning, and medical device development.

### 3.4. Windkessel Equation Formulation

The provided diagram illustrates a lumped parameter model representing a circulatory system, with a focus on the Windkessel effect. The components are defined as follows:

- Pump (e.g., Left Ventricle), generating pressure  $P_i$  (e.g., 80-120).
- $R_{ph, \text{minor}}$ : Minor peripheral resistance (appears to be excluded from main equations).
- $R_{\text{chamber}}$ : Resistance of the chamber (appears to be excluded from main equations).
- Flow Divider.

- $R_{\text{circulatory}}$  or  $R_{\text{circ}}$ : Characteristic/proximal resistance of the large arteries.
- $C_{\text{phantom}}$  or  $C$ : Compliance of the phantom/arterial system.
- $R_{\text{circ}}$  (labeled as  $R_c$  in a later step and in the image's equation line): Represents the characteristic resistance.
- $R_{\text{Peripheral}}$  or  $R_{\text{ph}}$ : Peripheral resistance (distal/systemic vascular resistance).
- Ground symbol (representing datum pressure).

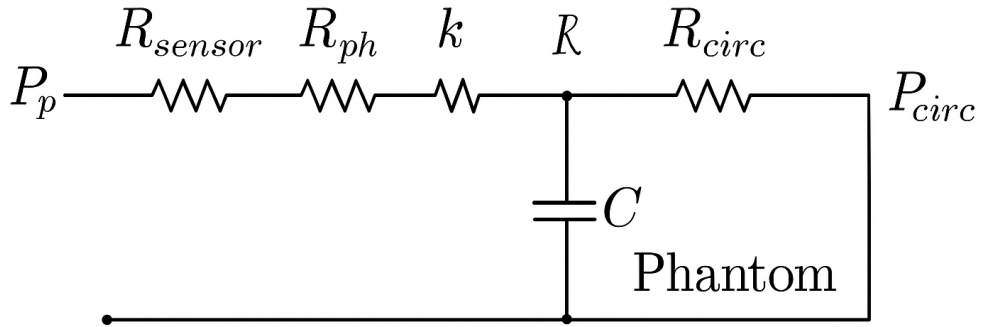


Figure 3.3: Lumped parameter model representing the circulatory loop including sensor resistance ( $R_{\text{sensor}}$ ), phantom inlet resistance ( $R_{\text{ph}}$ ), flow resistance ( $k$ ), compliance ( $C_{\text{phantom}}$ ), and downstream arterial resistance ( $R_{\text{circ}}$ ).

Let  $P_c$  be the pressure at the node between  $R_{\text{circulatory}}$  and the parallel combination of  $C$  and  $R_{\text{Peripheral}}$ . Let  $Q_{\text{circ}}$  be the flow through  $R_{\text{circulatory}}$ . Let  $Q_c$  be the flow through the capacitor  $C$ . Let  $Q_{\text{ph}}$  be the flow through the peripheral resistance  $R_{\text{ph}}$ .

From the diagram and handwritten notes, the following relationships can be derived:

## Equation for $R_{\text{circulatory}}$ ( $R_{\text{circ}}$ )

The pressure drop across  $R_{\text{circ}}$  is given by:

$$P_i - P_c = Q_{\text{circ}} R_{\text{circ}}$$

This implies the flow  $Q_{\text{circ}}$  into the compliance node is:

$$Q_{\text{circ}} = \frac{P_i - P_c}{R_{\text{circ}}} \quad (3.10)$$

## Equation for $R_{\text{ph}}$

The pressure drop across  $R_{\text{ph}}$  is simply the pressure at the node  $P_c$ :

$$P_c - 0 = Q_{\text{ph}} R_{\text{ph}}$$

Therefore, the flow  $Q_{\text{ph}}$  out of the compliance node is:

$$Q_{\text{ph}} = \frac{P_c}{R_{\text{ph}}} \quad (3.11)$$

## Equation for $C$ (Compliance)

The fundamental equation for a capacitor relates the current through it to the rate of change of voltage across it. Here,  $Q_c$  is the flow into the capacitor and  $P_c$  is the pressure across it:

$$Q_c = C \frac{dP_c}{dt} \quad (3.12)$$

## Continuity Equation at the Compliance Node

By applying the principle of conservation of flow (Kirchhoff's Current Law) at the node where  $R_{\text{circ}}$ ,  $C$ , and  $R_{\text{ph}}$  meet: Flow in ( $Q_{\text{circ}}$ ) = Flow out through compliance ( $Q_c$ ) + Flow out through peripheral resistance ( $Q_{\text{ph}}$ )

$$Q_{\text{circ}} = Q_c + Q_{\text{ph}}$$

Rearranging to find the rate of change of pressure  $dP_c/dt$ :

$$Q_c = Q_{\text{circ}} - Q_{\text{ph}}$$

Substituting the capacitor equation:

$$C \frac{dP_c}{dt} = Q_{\text{circ}} - Q_{\text{ph}}$$

Substituting the expressions for  $Q_{\text{circ}}$  and  $Q_{\text{ph}}$ :

$$C \frac{dP_c}{dt} = \frac{P_i - P_c}{R_{\text{circ}}} - \frac{P_c}{R_{\text{ph}}} \quad (3.13)$$

This is the main governing ordinary differential equation for the pressure at the compliance node ( $P_c$ ) in a 3-element Windkessel model. The handwritten notes further rearrange this:

$$\frac{dP_c}{dt} = \frac{1}{C} \left[ Q_{\text{circ}} - \frac{P_c}{R_{\text{ph}}} \right]$$

$$\frac{dP_c}{dt} = \frac{1}{C} \left[ \frac{P_i - P_c}{R_{\text{circ}}} - \frac{P_c}{R_{\text{ph}}} \right]$$

The expression  $P_c = P - R_{\text{ph}}Q$  represents the pressure at the compliance chamber ( $P_c$ ) as a result of the pressure drop across the peripheral resistance  $R_{\text{ph}}$ . It is derived under the assumption of steady-state or quasi-steady flow conditions, where the flow  $Q$  and upstream pressure  $P$  are known, and inertial and capacitive effects are negligible. This simplification is useful in contexts where the compliance element is assumed to respond instantaneously to pressure changes or when analyzing the mean flow behavior over time.

Another expression is presented for  $dP$ :

$$dP = R_{\text{ph}}[Q_{i+1} - Q_i] + \frac{\Delta t}{C} \left( Q_i - \frac{P_i - R_p h Q_i}{R_{\text{circ}}} \right)$$

This equation appears to be a finite difference or a specific form of a discrete-time update rule for pressure, possibly representing a numerical integration step for a lumped parameter model, where  $Q_{\text{in}}$  could be total inflow and  $Q_i$  some intermediate flow. Without more context, its direct derivation from the preceding continuous-time equations is unclear.

### 3.4.1. Experimental R–C Parameters in Human Systemic Arterial Models

Accurate parameterization of lumped Windkessel models requires experimental or clinically validated values of systemic vascular resistance ( $R$ ) and arterial compliance ( $C$ ). Several research groups have reported values for these parameters based on in vivo mea-

surements, data fitting, or physical modeling. Table ?? summarizes published values of resistance and compliance used in RC or RCR models of human systemic arteries.

Liu et al. [25] implemented a two-element Windkessel model (RC), reporting a systemic resistance in the range of  $R = 0.89$  to  $1.99 \text{ mmHg} \cdot \text{s/mL}$  and compliance between  $C = 0.47$  and  $1.86 \text{ mL/mmHg}$ . These values represent a simplified model of the arterial system, yet are widely used for coupling lumped models to upstream CFD domains.

Segers et al. [35] employed a more advanced model (denoted RLCR2) that includes proximal resistance ( $R_c$ ), characteristic resistance ( $R$ ), compliance ( $C$ ), and inertance ( $L$ ). Their reported range for  $R_c$  was  $0.035$  to  $0.109 \text{ mmHg} \cdot \text{s/mL}$ , and for  $R$  was  $0.82$  to  $1.15 \text{ mmHg} \cdot \text{s/mL}$ , with compliance  $C = 0.68$  to  $1.32 \text{ mL/mmHg}$  and inertance  $L = 0.005 \text{ mmHg} \cdot \text{s}/(\text{mL/s})$ . This multi-element setup better captures wave propagation effects.

Stergiopoulos et al. [38] presented both measured and fitted values for a three-element RCR model. The measured proximal resistance was  $R_c = 0.058$  to  $0.070 \text{ mmHg} \cdot \text{s/mL}$ , with total resistance  $R = 0.63$  to  $0.79 \text{ mmHg} \cdot \text{s/mL}$  and compliance  $C = 1.28$  to  $2.48 \text{ mL/mmHg}$ . Their fitted data provided slightly different parameters:  $R_c = 0.03$  to  $0.033 \text{ mmHg} \cdot \text{s/mL}$  and  $C = 1.75$  to  $5.16 \text{ mL/mmHg}$ , indicating sensitivity to the optimization method used.

Westerhof et al. [45] originally reported parameters in non-physiological units and later converted them into compatible values for hemodynamic modeling:  $R_c = 0.0675 \text{ mmHg} \cdot \text{s/mL}$ ,  $R = 0.9 \text{ mmHg} \cdot \text{s/mL}$ , and  $C = 1.067 \text{ mL/mmHg}$ . These values are often used in closed-loop modeling of cardiovascular physiology.

**Table 3.1: Published Experimental Data for Human Systemic Arterial Vasculature Models**

Model	Values in Physiological Units	Source
<b>RC</b>	$R = 0.89 \sim 1.99 \text{ mmHg} \cdot \text{s/mL}$ $C = 0.47 \sim 1.86 \text{ mL/mmHg}$	Liu et al. [25]
<b>RLCR2</b>	$R_c = 0.035 \sim 0.109 \text{ mmHg} \cdot \text{s/mL}$ $R = 0.82 \sim 1.15 \text{ mmHg} \cdot \text{s/mL}$ $C = 0.68 \sim 1.32 \text{ mL/mmHg}$ $L = 0.005 \text{ mmHg} \cdot \text{s}/(\text{mL/s})$	Segers et al. [35]
<b>RCR</b>	<i>In vivo measured:</i> $R_c = 0.058 \sim 0.070 \text{ mmHg} \cdot \text{s/mL}$ $R = 0.63 \sim 0.79 \text{ mmHg} \cdot \text{s/mL}$ $C = 1.28 \sim 2.48 \text{ mL/mmHg}$ <i>Data fitted:</i> $R_c = 0.03 \sim 0.033 \text{ mmHg} \cdot \text{s/mL}$ $R = 0.63 \sim 0.79 \text{ mmHg} \cdot \text{s/mL}$ $C = 1.75 \sim 5.16 \text{ mL/mmHg}$	Stergiopoulos et al. [38]
<b>RCR</b>	<i>Original values:</i> $R_c = 90 \text{ g}/(\text{cm}^4 \cdot \text{s})$ $R = 1200 \text{ g}/(\text{cm}^4 \cdot \text{s})$ $C = 8 \times 10^{-4} \text{ cm}^4 \cdot \text{s}^2/\text{g}$ <i>Converted into physiological units:</i> $R_c = 0.0675 \text{ mmHg} \cdot \text{s/mL}$ $R = 0.9 \text{ mmHg} \cdot \text{s/mL}$ $C = 1.067 \text{ mL/mmHg}$	Westerhof et al. [45]

The variation in reported values arises from differences in the target population (healthy vs. hypertensive), model assumptions (rigid vs. elastic vessels), and estimation approach (direct measurement vs. optimization). Nevertheless, these ranges provide a solid reference for tuning lumped parameter models in both numerical simulations and physical mock circulatory systems.

Crucially, modern MCL designs account for pressure losses across various components, including connectors, bends, or sensors, which can introduce minor pressure drops due

to friction or flow separation [48]. While often smaller than the main resistance valve, these distributed resistances can cumulatively affect the loop's overall characteristics. Parker et al. [30] demonstrated that even nominally identical devices can exhibit differing pressure-flow characteristics due to variations in length, diameter, and geometry. In practice, MCL builders minimize such losses by using short, wide connectors and gentle curves, or by incorporating their effect into the Windkessel model's "proximal resistance" [48]. A recent open-loop MCL study by Hong et al. [18] even highlighted the importance of eliminating unintended pressure drops (e.g., from gravity in vertical loops) to maintain physiological pressure levels. This meticulous attention ensures that the Windkessel elements ( $C$  and  $R$ ) can be accurately tuned to match human hemodynamics without unexpected pressure drops from the setup. Recent reviews confirm that a properly configured Windkessel-based MCL can reliably reproduce normal aortic pressure waveforms (e.g., 120/80) and flow rates, providing a robust testbed for cardiovascular devices [48].

### 3.5. Pressure waive and its effect on compliance

As shown in the figure, the aorta and arteries have the highest blood pressure. The mean aortic pressure (solid red line) is about 90 mmHg in a resting individual with normal arterial pressures. The mean blood pressure does not fall very much as the blood flows down the aorta and through large distributing arteries. It is not until the small arteries and arterioles that there is a large fall in mean blood pressure. Approximately 50-70% of the pressure drop along the vasculature occurs within the small arteries and arterioles because of their large contribution to systemic vascular resistance. By the time blood reaches the capillaries, the mean pressure may be 25-30 mmHg, depending on the organ. The pressure falls further as the blood travels into the veins and back to the heart. Pressure within the thoracic vena cava near the right atrium is very close to zero and fluctuates from a few mmHg negative to positive with respiration.[20]

The arterial pulse pressure (shown as the gray band around the mean pressure in the figure) increases as the blood flow travels down the aorta and into distributing arteries. The systolic pressure rises and the diastolic pressure falls, therefore the pulse pressure increases. This occurs because of reflective waves from vessel branching and from decreased arterial compliance (increased vessel stiffness) as the pressure pulse travels from the aorta into distributing arteries. As the blood flows into smaller arteries and arterioles, the pulsatility declines.

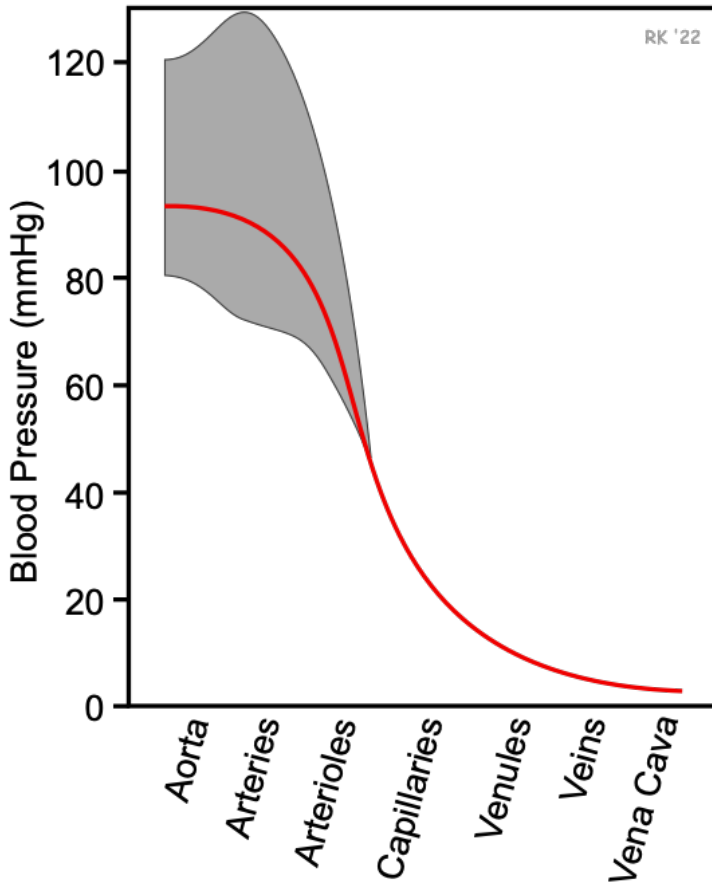


Figure 3.4: Circulatory Blood pressure(From Left ventricle to Vena Cava)[20]

Cardiac output and systemic vascular resistance undergo large changes with physical activity, and these changes result in a redistribution of pressures and volumes, as well as blood flow, within the circulatory system.

## 3.6. Imaging and 3D Printing of the Aortic Phantom

### 3.6.1. Imaging and segmentation

This section outlines the imaging source, segmentation process, and surface modeling techniques used to generate the 3D-printed aortic phantom. Starting from contrast-enhanced CT data, a detailed model of the thoracoabdominal aorta was obtained, cleaned, and adapted for integration into the compliance chamber.

The original aortic geometry was extracted from a high-resolution computed tomography angiography (CTA) dataset covering the thoracic and abdominal regions. The CT acquisition included multiple contrast phases, enhancing both lumen visibility and soft tissue

differentiation. To prepare for segmentation, images were resampled to isotropic voxel spacing and intensity-normalized. Rigid registration ensured consistent alignment across contrast phases.

Using a combination of semi-automated tools—including intensity thresholding, region growing, and manual correction—masks of the aortic lumen and its branches were created. The segmentation encompassed major aortic branches including the brachiocephalic trunk, left common carotid, left subclavian, celiac trunk, superior mesenteric artery (SMA), bilateral renal arteries, and the iliac bifurcation. A sample of the fully segmented aorta is shown in Figure 3.5.



**Figure 3.5: Initial 3D model of the full aorta with all major branches.** Segmented from contrast-enhanced CT images using a multi-mask approach.

After initial segmentation, the model was exported as an STL surface mesh and processed to enhance its usability for physical modeling. A Laplacian surface wrapping algorithm was applied to smooth stair-step artifacts and fill small holes, resulting from segmentation

imperfections.

To make the model compatible with the dimensions and constraints of the compliance box, unnecessary peripheral branches were removed, and the geometry was trimmed. Specifically, the model was shortened above the aortic arch and below the iliac bifurcation to reduce its length while maintaining anatomical relevance. Furthermore, side branches not critical to the target hemodynamic behavior were excluded to simplify downstream flow simulations.

The cleaned model, shown in Figure 3.6, preserves the main curvature and caliber of the aorta while offering a watertight, smoothed geometry ideal for 3D printing and compliance analysis.



**Figure 3.6: Cleaned and trimmed aortic model used in the physical phantom.**  
Non-essential branches were removed

### 3.6.2. Anatomical Variation in Aortic Morphology

The human aorta demonstrates substantial variability in morphology, including differences in diameter, length, curvature, and angulation, particularly within the aortic arch region. These morphological characteristics are significantly influenced by factors such as age and sex, making their detailed analysis clinically relevant for patient-specific management of thoracic aortic pathologies and endovascular interventions.

Boufi et al. (2017)[5] conducted a detailed morphological analysis of the aortic arch in a healthy adult population using computed tomography angiography (CTA). This study provides comprehensive morphometric and geometric parameters, including aortic diameters, lengths, angles, curvature radii, and tortuosity indices. These parameters were quantitatively assessed, revealing their significant variability across different zones of the aorta and correlations with demographic factors.

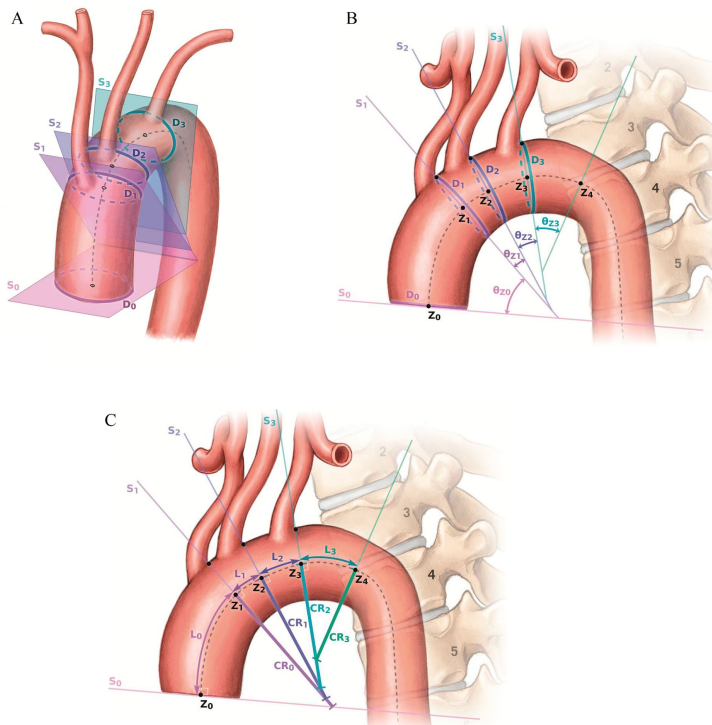


**Figure 3.7:** Standardized morphological parameters and reference planes of the aortic arch, adapted from [6].

Figure 3.2 illustrates the standardized morphological and geometric parameters used to characterize the aortic arch according to Boufi et al. (2017). Panel (A) demonstrates the four transverse reference planes (S0–S3) corresponding to zones Z0 to Z3, used to measure diameters (D<sub>0</sub> to D<sub>3</sub>). Panel (B) defines the angular parameters ( $\theta_{Z0}$ ,  $\theta_{Z1}$ ,  $\theta_{Z2}$ , and  $\theta_{Z3}$ ), which quantify aortic arch angulations at each corresponding zone. Panel (C)

represents the lengths of each zone ( $L_0$  to  $L_3$ ), total arch length ( $L_{arch}$ ), and curvature radii (CR) along the aortic centerline, highlighting the complex geometric configuration and tortuosity of the aortic arch.

The diameter of the aorta decreases progressively from the ascending aorta to the descending segment, with average diameters ranging from approximately 30 mm proximally to about 25 mm distally. The aortic arch shows zone-specific variations in curvature and length, with posterior segments typically exhibiting greater elongation with advancing age, accompanied by decreases in global tortuosity but increases in local curvature radii. These changes are critical for preoperative planning, especially in thoracic endovascular aortic repair (TEVAR), where accurate morphological characterization can improve the outcomes of interventions.

## Morphometric and Geometric Parameters

Table 3.2 summarizes key morphometric and geometric parameters measured in the healthy population, providing a reference baseline for clinical assessments.

### 3.6.3. 3D Printing of the Aortic Phantom

The cleaned STL file of the aortic geometry was directly 3D printed at IRCCS Policlinico San Donato using a hyperelastic VisiJet material, selected for its excellent compliance and anatomical accuracy. The printing was performed using MultiJet Printing (MJP) technology on high-resolution printers (e.g., ProJet2500/3600 series), which offer a layer thickness of approximately 50m—sufficient to accurately capture the complex morphology of vascular structures.

VisiJet CE-BK (black) and CE-NT (natural), members of 3D Systems' hyperelastic elastomer family, were utilized for their favorable mechanical properties. With a low tensile strength of approximately 0.2–0.4MPa and pronounced elastic behavior, these materials closely mimic the mechanical characteristics of vascular walls under pulsatile flow conditions.

Layer resolution was maintained between 50–100m to ensure smooth lumen surfaces and well-defined branching. Wall thickness was carefully controlled to replicate physiological elasticity. Light support structures were used during printing and subsequently removed to preserve the integrity of the thin-walled geometry. Quality control included visual and dimensional inspection at key anatomical landmarks, along with manual deformation tests to confirm the expected compliance of the printed phantom.

**Table 3.2:** Morphometric and geometric parameters of the healthy aortic arch (mean  $\pm$  SD), adapted from [6].

Parameter	Healthy Control Group (n = 123)
<b>Morphometric</b>	
$D_0$ (mm)	30 $\pm$ 0.71
$D_1$ (mm)	28 $\pm$ 0.71
$D_2$ (mm)	26 $\pm$ 0.71
$D_3$ (mm)	25 $\pm$ 0.53
$\theta_{Z0}$ (°)	46 $\pm$ 2.3
$\theta_{Z1}$ (°)	13 $\pm$ 1.24
$\theta_{Z2}$ (°)	23 $\pm$ 1.41
$\theta_{Z3}$ (°)	35 $\pm$ 3.0
$\theta_{arch}$ (°)	107 $\pm$ 2.65
$L_0$ (mm)	30 $\pm$ 1.24
$L_1$ (mm)	8 $\pm$ 0.71
$L_2$ (mm)	15 $\pm$ 0.71
$L_3$ (mm)	19 $\pm$ 1.77
$L_{arch}$ (mm)	71 $\pm$ 2.65
<b>Geometric</b>	
Tortuosity Index (TI)	1.19 $\pm$ 0.01
Arch width (mm)	60 $\pm$ 2.12
Curvature Radius $CR_0$ (mm/rad)	39 $\pm$ 1.77
Curvature Radius $CR_1$ (mm/rad)	41 $\pm$ 4.24
Curvature Radius $CR_2$ (mm/rad)	39 $\pm$ 3.71
Curvature Radius $CR_3$ (mm/rad)	34 $\pm$ 2.12
Curvature Radius $CR_{arch}$ (mm/rad)	39 $\pm$ 1.41
Attachment angle $\alpha_{Z1}$ (°)	154 $\pm$ 1.77
Attachment angle $\alpha_{Z2}$ (°)	155 $\pm$ 1.77
Attachment angle $\alpha_{Z3}$ (°)	153 $\pm$ 1.59



**Figure 3.8: 3D-printed aortic phantom.** Directly printed in hyperelastic VisiJet CE elastomer on a high-resolution MJP printer at SanDonato Hospital.

The resulting phantom exhibits a non-realistic mechanical response under flow and pressure, failing in displaying accurate in-vitro compliance testing excluding Mock circulatory loop.



# 4 | Results

## 4.1. Governing Equation Overview

In modeling the aortic compliance, the human aorta was approximated as a cylindrical tube under physiological internal pressure. Considering the thin-wall assumption, the hoop stress (circumferential stress) dominates and can be described through classical thin-wall pressure vessel equations. This assumption is justified due to the significantly greater radius-to-thickness ratio in physiological and phantom conditions.

The choice of a hyperelastic material model is necessary to accurately capture the non-linear elastic response of biological tissues, such as the aorta, which undergo large strains and deformations under physiological conditions. Among the available hyperelastic models, the Mooney-Rivlin model was selected due to its established ability in the literature to accurately represent biological soft tissues' mechanical behavior, particularly vascular tissues, under a broad range of deformation conditions [16]. This choice enables capturing both the linear and nonlinear elastic behavior typically observed in aortic tissues and phantom models.

Starting with the Mooney-Rivlin constitutive equation, the strain in the radial and axial directions was simplified and substituted entirely into circumferential strain terms. This simplification is valid given the dominance of circumferential deformation due to internal blood pressures. The circumferential stretch, denoted as  $\lambda_\theta$ , relates directly to the diameter changes as:

$$\lambda_\theta = \frac{D}{D_0} \tag{4.1}$$

where  $D$  is the current diameter and  $D_0$  is the original reference diameter. Notably,  $\lambda_\theta$  directly corresponds to the physiological concept of distensibility, extensively discussed in the literature review. Physiological distensibility ranges were well-documented, allowing  $\lambda_\theta$  to serve as a reliable benchmark for modeling compliance.

Having derived the fundamental relationships, the final equation that relates internal

pressure ( $P_{\text{in}}$ ), external water pressure and air volume conditions to aortic compliance was obtained. This comprehensive equation innovatively links the physiological behavior of the aortic phantom to controllable experimental parameters:

$$P_{\text{in}} - \left( \frac{P_0 V_0}{V_0 - \frac{\pi}{4} D_0^2 \lambda_\theta^2 (\lambda_\theta^2 - 1)} + \rho g h \right) = \frac{4(C_1 + C_2)t_0}{\lambda_\theta^2 D_0} \left( \lambda_\theta^2 - \frac{1}{\lambda_\theta^2} \right) \quad (4.2)$$

In this equation:

- $P_{\text{in}}$  represents the internal pressure applied by the pump (physiological pressure simulation).
- $P_0$  and  $V_0$  represent the initial air pressure and volume within the compliance-controlled chamber.
- $\rho g h$  accounts for the hydrostatic pressure exerted by the water column, dependent on the water level ( $h$ ).
- $C_1$  and  $C_2$  are Mooney-Rivlin material constants characterizing the hyperelastic behavior of the aortic phantom.
- $t_0$  is the initial thickness of the phantom wall.

Two variables—initial pump pressure ( $P_{\text{in}}$ ) and water level ( $h$ )—were explicitly chosen as the primary design parameters for practical feasibility and ease of control. By setting physiological targets for  $\lambda_\theta$ , this equation allows explicit determination of all other design parameters required to achieve desired compliance behaviors in the proposed experimental setup. Detailed solutions and analyses of this equation utilizing MATLAB are presented in subsequent sections, providing graphical relationships and parametric insights for the comprehensive understanding and design of the compliance-controlled system.

## 4.2. Compliance and Distensibility

To evaluate the behavior of the aortic phantom under varying physiological conditions, the derived governing equation (Equation 4.2) was solved numerically in MATLAB. The simulation explored the effects of pump pressure ( $P_{\text{in}}$ ) and water column height ( $h$ ) on stretch ratio ( $\lambda_\theta$ ), internal air pressure ( $P_{\text{air}}$ ), volume changes, and overall compliance. The analysis involved sweeping a range of pressures and water heights, and recording the resulting biomechanical responses of the phantom.

#### 4.2.1. Simulation Parameters and Definitions

Before performing the numerical simulation of the governing equation, all relevant physical and geometrical parameters were defined and are summarized in Table 4.1. These include constant properties such as fluid density and gravitational acceleration, geometrical features of the aortic phantom, and material-specific parameters derived from uniaxial tests fitted to the Mooney-Rivlin hyperelastic model. In addition, two experimentally controllable variables—*pump pressure* ( $P_{in}$ ) and *water height* ( $h$ )—were selected as primary design parameters due to their direct influence on the mechanical behavior of the system.

The phantom diameter ( $D_0$ ), wall thickness ( $t_0$ ), and length ( $L$ ) were fixed based on common dimensions for in vitro aortic models. The initial air volume ( $V_0$ ), which varied with water height in the chamber, was dynamically computed within the simulation for each configuration. All pressures were treated in absolute terms and converted as needed using the mmHg-to-Pascal conversion factor.

Of particular importance are the two Mooney-Rivlin material constants ( $C_1$  and  $C_2$ ), which dictate the nonlinear elastic response of the phantom. These were extracted from curve-fitting procedures applied to experimental stress-strain data(uniaxial tests) and are critical in computing the elastic pressure contribution.

The circumferential stretch ratio ( $\lambda_{theta}$ ), a key output of the model, represents the relative increase in diameter and directly reflects aortic distensibility, which was the central target of the analysis.

Table 4.1 provides a comprehensive overview of all parameters used in the simulation, including their physical meaning, units, and roles in the governing equation or design process.

Table 4.1: List of Parameters Used in MATLAB-Based Parametric Analysis

Parameter	Value / Range	Unit	Notes
$P_{in}$	80–120	mmHg	Internal pump pressure (design variable)
$h$	0–20	cm	Water column height (design variable)
$P_0$	760	mmHg	Atmospheric pressure in the chamber
$V_0$	100–500	mL	Initial air volume; affects external pressure response
$D_0$	25	mm	Initial diameter of aorta phantom
$t_0$	2	mm	Initial wall thickness of the phantom
$\lambda_\theta$	1.0–1.2	—	Circumferential stretch ratio (computed)
$\rho$	1000	kg/m <sup>3</sup>	Density of water
$g$	9.81	m/s <sup>2</sup>	Gravitational acceleration
$C_1$	0.022318	MPa	Mooney-Rivlin material constant (fitted from uniaxial data)
$C_2$	0.016764	MPa	Mooney-Rivlin material constant (fitted from uniaxial data)

#### 4.2.2. Variation of Compliance with diastolic-systolic pressure

Figure ?? shows the variation in aortic phantom compliance as a function of physiological arterial pressure, ranging from 80 to 120 mmHg — representative of diastolic to systolic conditions. The compliance is evaluated for four distinct water column heights in the external chamber: 8 cm, 12 cm, 16 cm, and 19 cm. This water level controls the external load applied to the phantom, simulating the extravascular environment.

As observed, lower water levels (e.g., 8 cm) are associated with significantly higher compliance values, reaching nearly 2.0 mL/mmHg at 120 mmHg. This suggests that the phantom undergoes greater volumetric expansion under pulsatile pressure when the ex-

ternal constraint is minimized, closely resembling a healthy, elastic arterial wall. The linear trend with increasing pressure is consistent with the elastic response expected in compliant vessels under physiological conditions.

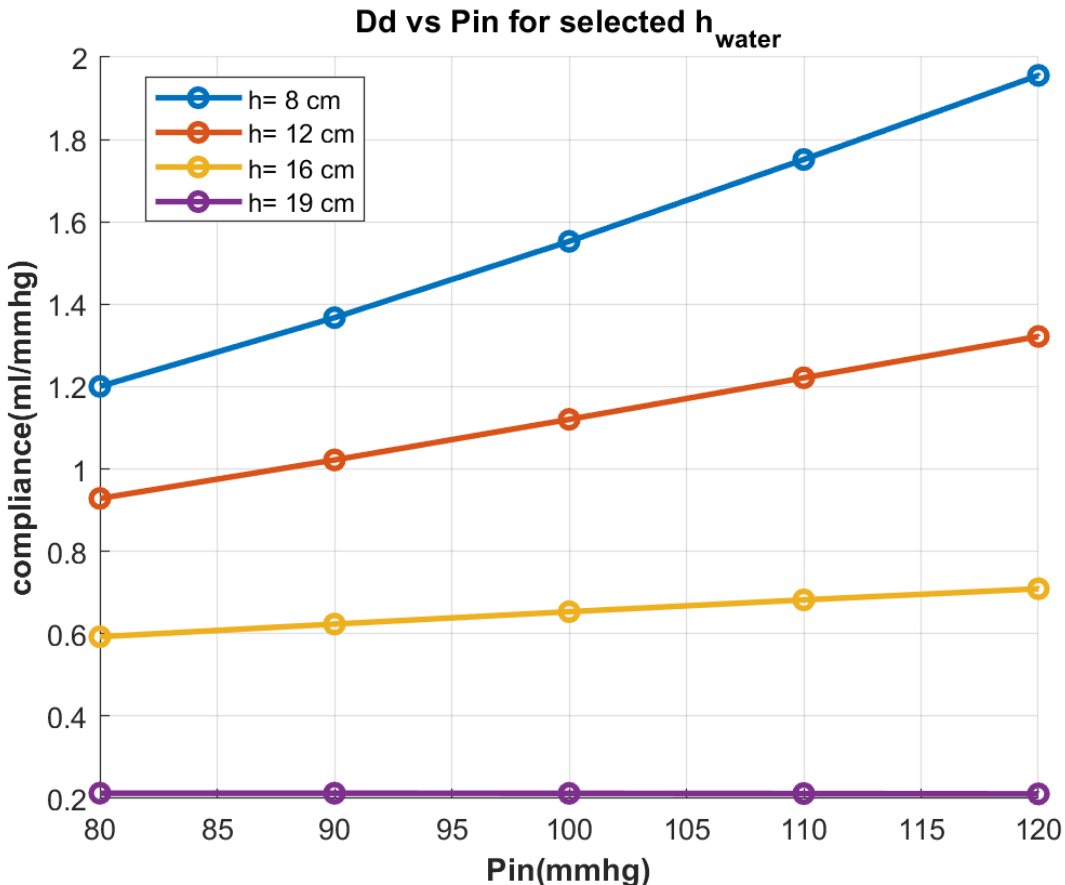


Figure 4.1: Compliance of the aortic phantom as a function of physiological pressure for various external water heights.

Conversely, at higher water levels (e.g., 19 cm), compliance remains consistently low across the entire pressure range, staying below 0.3 mL/mmHg. This indicates a stiffer response, where the vessel is significantly constrained by the surrounding medium, limiting its ability to expand — a condition that may simulate pathological states such as vascular calcification or increased external pressure in clinical scenarios.

Intermediate heights (12 cm and 16 cm) produce moderate compliance responses, showing a transition from elastic to more restricted deformation as water level increases. Importantly, the compliance range between 1.0–1.6 mL/mmHg seen at 12 cm aligns well with typical values reported for the human thoracic aorta, reinforcing the physiological relevance of the chosen design parameters.

In summary, this result highlights the critical role of external mechanical environment in modulating aortic compliance and supports the design's ability to replicate both healthy and pathological vascular behaviors by simply adjusting the surrounding water level.

#### 4.2.3. Distensibility Response to Arterial Pressure

Figure 4.2 illustrates the relationship between volumetric distensibility ( $Dv$ ) and arterial pressure ( $P_{in}$ ), a critical indicator of vascular elasticity. Volumetric distensibility, defined as the fractional change in volume per unit pressure (1/mmHg), characterizes the capacity of the aortic phantom to deform and store blood during cardiac cycles, closely mimicking the elastic behavior observed in the physiological aorta.

The presented data indicate a clear dependence of distensibility on external water height. Specifically, the phantom displays greater volumetric distensibility at lower external water heights (e.g., 8 cm and 12 cm), implying reduced external mechanical constraints and greater compliance resembling healthy arterial conditions. Conversely, increasing external water height significantly reduces distensibility, reflecting a stiffer response similar to pathological states such as vascular stiffening seen in hypertension or arterial aging.

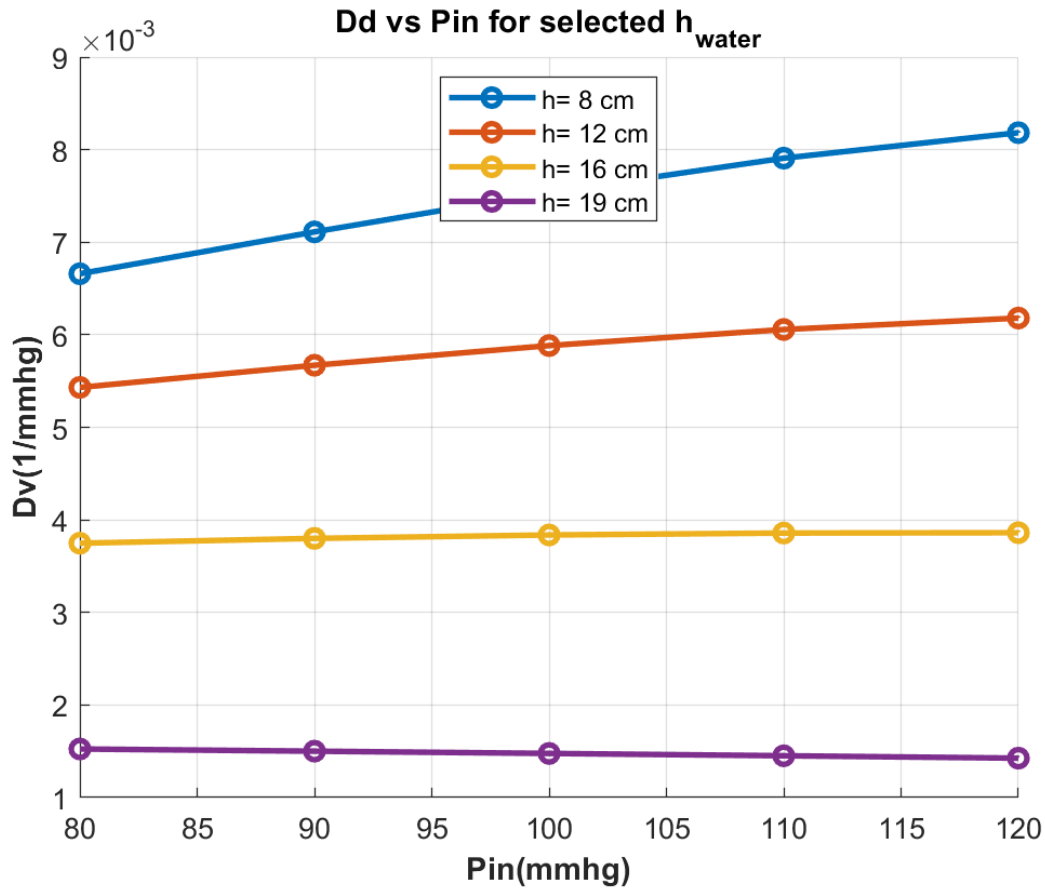


Figure 4.2: Volumetric distensibility ( $D_v$ ) of the aortic phantom as a function of physiological arterial pressure ( $P_{in}$ ) at various external water heights.

To contextualize these findings, physiological aortic distensibility values from the literature have been summarized in Table 4.2, facilitating direct comparison with the modeled phantom responses:

Table 4.2: Physiological Aortic Distensibility Values from Literature

Aortic Region	Distensibility ( $10^{-3} \text{ 1/mmHg}$ )	Reference
Thoracic Aorta	5.9 – 7.2	Boutouyrie et al. (1992) [7]
Ascending Aorta	3.8 – 6.5	Laurent et al. (2006) [23]
Thoracic Aorta	4.2 – 8.1	Redheuil et al. (2010) [32]
Abdominal Aorta	3.0 – 5.5	Stefanadis et al. (1993) [37]

Comparing the experimental phantom results to these physiological values, the modeled

distensibility at water heights of 8 cm and 12 cm closely aligns with the physiological range reported for the thoracic and ascending aorta, underscoring the biological relevance and accuracy of the designed phantom. At higher external constraints (16 cm and 19 cm water height), the decreased distensibility values observed are indicative of conditions characterized by reduced arterial elasticity, such as advanced age or vascular disease.

Thus, these results affirm the potential of the designed phantom to accurately simulate a wide spectrum of physiological and pathological aortic conditions, making it a valuable tool for experimental cardiovascular studies and medical device testing.

#### 4.2.4. Circumferential Stretch Ratio ( $\lambda$ ) as a Function of Pump Pressure

The circumferential strain, denoted as  $\lambda$ , represents the ratio of the deformed diameter to the initial diameter. Physiologically, the human aorta typically undergoes about a 20% increase in diameter during systolic pressure, corresponding to a value of approximately 1.2 [14, 26]. This strain range is crucial for maintaining healthy cardiovascular dynamics, as deviations can indicate pathological conditions such as aneurysms or arterial stiffening [2].

Figure 4.3 demonstrates the relationship between circumferential strain and internal pressure, under varying external water column heights. At an  $\lambda$  value of 8 cm, ranges from approximately 1.20 at 80 mmHg to 1.44 at 130 mmHg, closely approximating the physiological compliance range observed *in vivo* [43]. As external water height increases, circumferential strain significantly decreases, highlighting the direct impact of external pressure on the aorta phantom's compliance. For instance, at 16 cm, the strain remains around 1.05 to 1.07, reflecting a much stiffer configuration that diverges from physiological conditions.

From the analysis, we observe that maintaining an external water height between approximately 8 to 12 cm yields circumferential strain values most congruent with physiological data. This indicates the optimal combination of water and air pressures to simulate the compliance of an actual human aorta accurately within the experimental closed box environment. Indeed, our prior analyses depicted in Figures X and Y support these findings, where compliance matched the known physiological distensibility values closely at these water heights.

Comprehensively, these findings underscore the importance of precisely controlling external pressures within phantom experiments to authentically replicate cardiovascular com-

pliance. Ultimately, this precise tuning is critical for advancing cardiovascular research, validating medical devices, and improving pre-surgical simulations [24, 41].

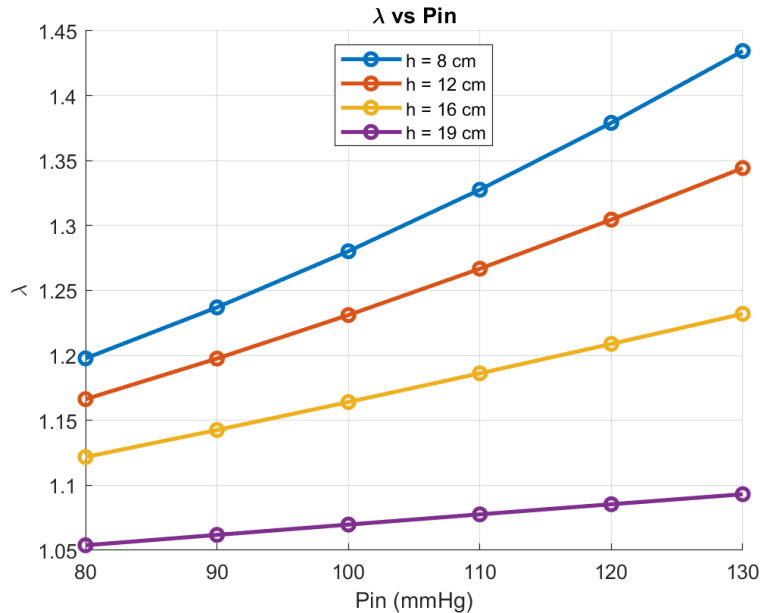
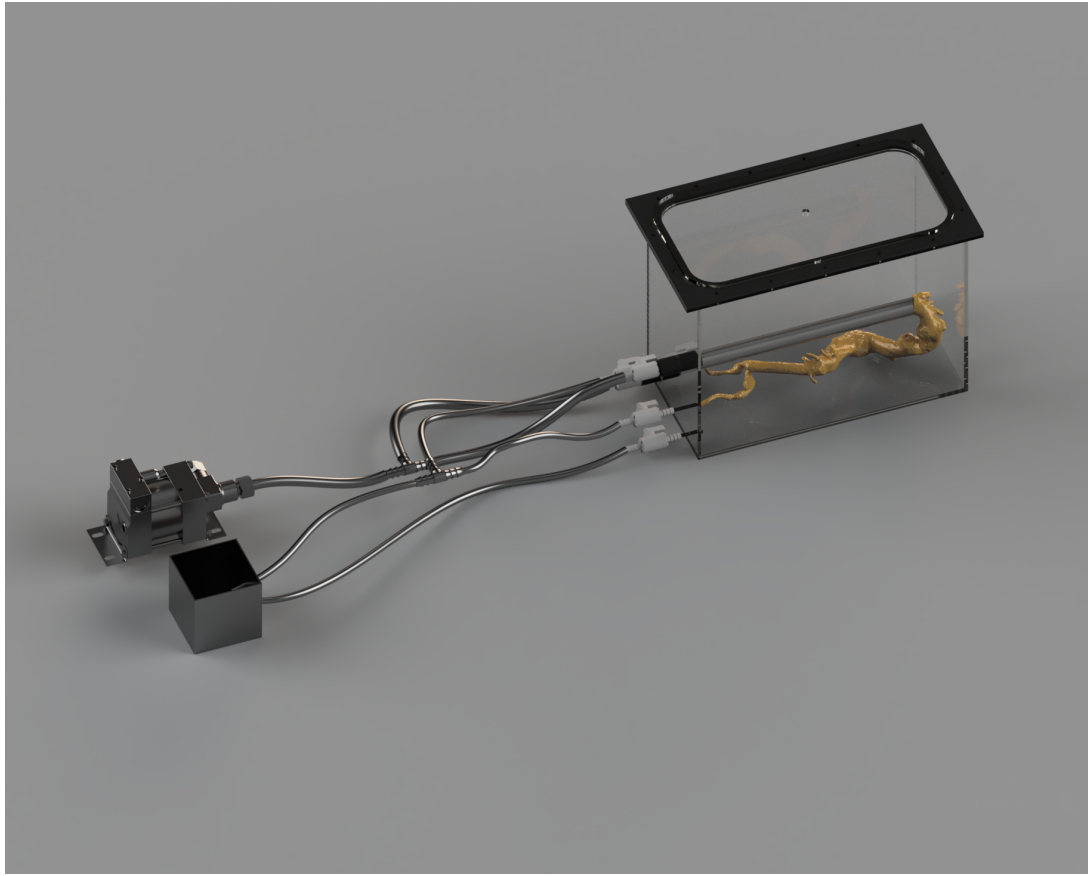


Figure 4.3: Circumferential strain as a function of internal pressure under different external water heights

### 4.3. Design of the Compliance-Controlled Chamber

The complete design of the mock circulatory loop is illustrated in Figure 4.4. This closed-loop system was developed to replicate the hemodynamic environment of the human aorta under controlled experimental conditions. The central component is a realistic, patient-specific aorta phantom housed within a custom-designed pressure chamber, enabling external pressurization to simulate physiological compliance.



**Figure 4.4: Complete mock circulatory loop.** The system includes the pressurizable compliance box housing the aorta phantom, inlet and outlet tubing, valves (Taps 1–5), a volumetric-flow pump, and connection points for pressure sensors. The layout enables control of fluid flow, adjustment of chamber water level.

The chamber features modular inlet and outlet interfaces, supported by a series of 2-way and 3-way valves, which allow for dynamic control of flow direction, water level adjustment, and system drainage. A single air-powered constant-flow pump drives the fluid through the phantom and also facilitates chamber pressurization by selectively redirecting flow using valve switches. The loop includes dedicated pressure measurement points at the ascending aorta and both iliac branches, where pressure catheters or sensors may be inserted. All components were dimensioned to maintain structural integrity under pressurized conditions, with O-ring seals and mechanical clamps ensuring airtightness. This integrated design enables flexible experimentation for investigating aortic compliance, pressure waveforms, and the effects of pathological geometries under physiologically relevant flow conditions.

Table 4.3: Components of the Experimental Setup

Component	Description and Function
<b>Clamp</b>	Glued to the box; contains a groove for a 5 mm O-ring ensuring a tight seal.
<b>O-ring</b>	5 mm cross-sectional diameter, fitted to a 160 mm perimeter groove for sealing.
<b>Box</b>	Enclosure for the aorta phantom; dimensioned for optimal pressure and compliance(Cross section=50*30).
<b>Connection Box–Phantom</b>	Cylindrical tube at inlet/outlet, glued for secure attachment to hoses.
<b>Barbed Tube Fitting</b>	Commercial PVC fitting for leak-proof fluid connections.Imported from MCmaster
<b>On–Off Valve</b>	Dark gray PVC valve used to control fluid flow through branches.
<b>Volumetric Flow Pump</b>	Air-powered pump maintaining steady physiological flow rates.
<b>Aorta Phantom</b>	3d printed Realistic anatomical model used for compliance testing and flow simulation.

Table 4.4: Components of the Experimental Setup for Aorta Phantom Testing.

### 4.3.1. Inlet-Outlet and sensors Configuration

The fluidic system is equipped with one primary inlet and two outlets integrated into the aortic phantom circuit. The main inlet, with an inner diameter of 2.5 cm, delivers the working fluid directly into the ascending aorta region of the phantom, replicating physiological flow entry. The two outlets, each with a diameter of 0.5 cm, simulate the branching of the renal arteries and guide the flow out of the phantom into the surrounding chamber. These dimensions reflect the anatomical disparity between the aortic trunk and its smaller branches.

Figure 4.5 illustrates the complete mock circulatory loop inlet and outlet, including the inlet and outlet setup previously discussed. The system is driven by a single pump, which

serves two distinct functions: (1) circulating fluid through the aortic phantom and (2) regulating the water level inside the compliance chamber.

Figure 4.5.

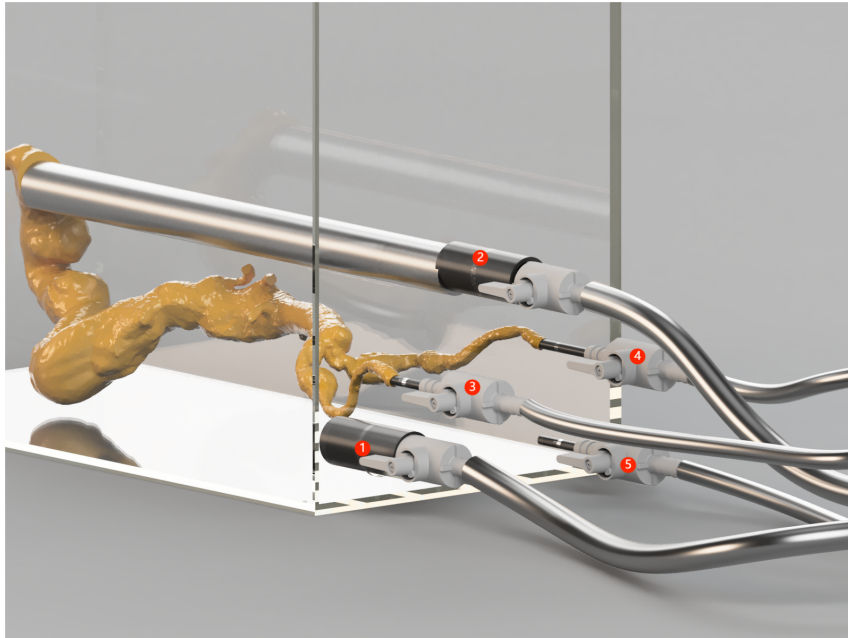


Figure 4.5: Inlet and Outlet of box, Including the connection tubes

To adjust the water level within the chamber, Tap 2 (inlet to the phantom) is closed while Tap 1 is opened. In this configuration, the pump directs fluid into the box to reach the desired water level. Conversely, to decrease the water level, Tap 5 is opened, allowing fluid to exit the box and flow into the free-surface reservoir due to gravitational drainage.

Tap 3 and Tap 4 correspond to the outlets of the iliac branches and remain open during the operation to allow continuous flow. These locations are also suitable for the placement of pressure sensors. Ideally, pressure catheters should be inserted directly inside the box at the terminal ends of the iliac branches to capture accurate internal pressure readings. However, from a fabrication perspective, positioning the sensors externally is considerably more practical and allows for easier maintenance and sealing.

Another key location for pressure monitoring is the ascending aorta, which is entirely enclosed within the chamber. To enable measurement at this site, a catheter is introduced through a dedicated opening in the lid, initially designed for a manometer. This allows direct access to the aortic root for capturing proximal pressure waveforms.

Additional pressure sensor placements may be considered based on experimental requirements. For instance, in [3], multiple sensors were distributed along the aortic path to

evaluate the influence of abdominal aortic aneurysms (AAA) on pressure profiles within flexible phantoms. The final decision on sensor positioning should be determined after system fabrication, taking into account structural constraints, sealing considerations, and the intended experimental objectives.

Table 4.5: Connection Ports of the Compliance Chamber refering Figure 4.5

ID	Diameter (cm)	Function
1	2.5	Water–inlet port for filling the compliance chamber.
2	2.5	Primary flow inlet conveying the pump output to the ascending-aorta section of the phantom.
3	0.5	Outlet returning flow from the first renal-artery branch to the chamber free surface.
4	0.5	Outlet returning flow from the second renal-artery branch to the chamber free surface.
5	0.5	Water–outlet port for lowering the chamber’s water level.

For each port, a dedicated connection tube—a cylindrical adapter 5 cm in length—is affixed to the external surface of the chamber using medical-grade adhesive. These adapters facilitate the attachment of silicone hoses or the aortic phantom via adjustable clamps or belts, ensuring a secure and leak-proof interface. The assembly is illustrated in

### 4.3.2. Lid Design and Sealing Mechanism

To allow for easy access to the internal components of the chamber—both for assembly (e.g., positioning the aorta phantom) and for routine maintenance or cleaning—a removable lid was designed for the top of the pressure box. Given the need to maintain a pressurized air environment within the chamber, it was essential to ensure an airtight seal between the lid and the box.

The sealing strategy involves a two-part clamp system, in which a custom-designed bottom clamp is permanently affixed to the upper edge of the box. This clamp, bonded with adhesive along both its inner and outer faces, provides a rigid base structure to ensure mechanical stability.

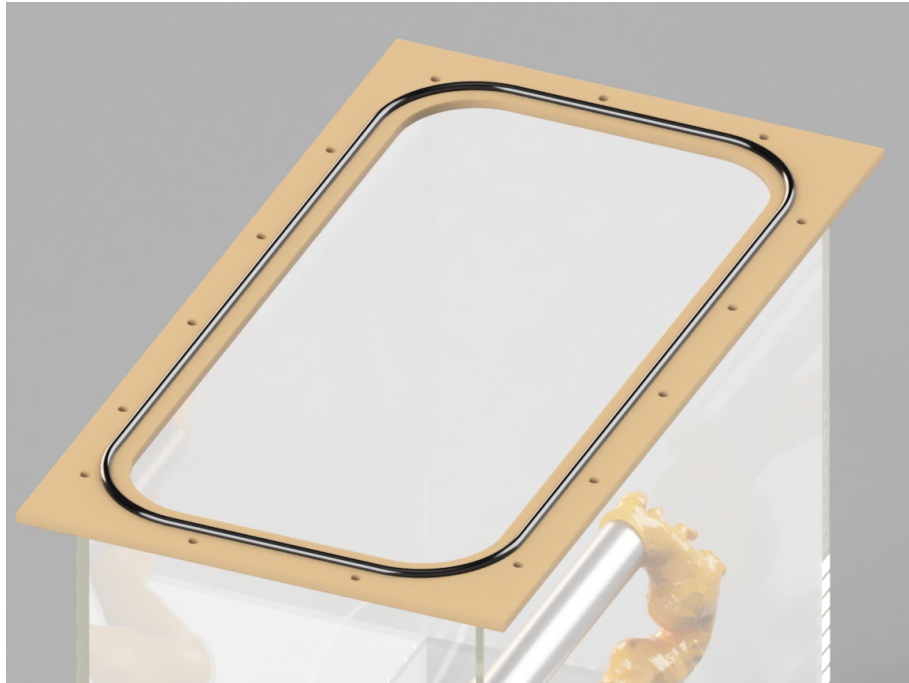


**Figure 4.6: Lid and Clamp Assembly for the Compliance Chamber.** The lid is secured to the top clamp using uniformly distributed M5 screws. An O-ring with a 5 mm cross-section is placed in a filleted groove to prevent sharp-edge contact and ensure airtight sealing under pressure. The bottom clamp is permanently glued to the box and serves as a structural interface for the lid.

On top of this clamp, a removable lid is placed and secured. To ensure airtightness under pressure, an O-ring groove was integrated into the upper face of the clamp based on mechanical design standards for dynamic seals. A 5 mm-thick O-ring was selected, and to avoid localized stress concentrations or cutting of the rubber, all groove edges were filleted. From a mechanical perspective, approximately 50 percent of the O-ring cross-section is seated in the groove, while the remaining half is compressed by the downward force of the lid, ensuring uniform contact and sealing under pressure.

To maintain this compression and mechanical integrity during operation, a series of M5 screws were used to bolt the lid onto the clamp. The number and spacing of these screws were chosen to guarantee uniform load distribution and to avoid deformation of the sealing surface.

This combined design—consisting of a glued clamp, a precision-machined O-ring groove, and a bolted lid—ensures both reusability and reliable airtight performance. A visual representation of the clamp and sealing mechanism is shown in Figure 4.6, and the geometric and material specifications of all related components are detailed in Table Y.

## 4.4. Circulatory Hemodynamic Analysis Via LPM Modeling

In order to calculate the total hydraulic resistance  $R_{\text{tot}}$  of the phantom, three pressure sensors must be placed strategically along the flow path:

- **Sensor 1 (Inlet):** Located at the ascending aorta, immediately distal to the left-ventricular outflow region. This measures the pressure experienced by the compliant element and defines the entry pressure,  $P_{\text{in}}$ .
- **Sensor 2 (Mid-point):** Positioned at the suprarenal abdominal aorta, proximal to the renal arteries. This allows resolution of the proximal conduit pressure drop and separates the pre- and post-AAA regions.
- **Sensor 3 (Outlet):** Installed at one of the common iliac artery terminations. This captures the outlet pressure,  $P_{\text{out}}$ , used for full-path  $\Delta P$  evaluation.

Under steady-state flow conditions (non-pulsatile), the total resistance is given by:

$$R_{\text{tot}} = \frac{P_{\text{in}} - P_{\text{out}}}{Q} \quad (4.3)$$

where  $Q$  is the volumetric flow rate [L/min or  $\text{m}^3/\text{s}$ ], measured using a calibrated flow sensor.

### 4.4.1. Decomposition of Total Resistance Components

To verify the hemodynamic accuracy of the mock circulatory loop, it is essential to analytically estimate the total hydraulic resistance of the phantom. This total resistance,  $R_{\text{tot}}$ , reflects both linear (distributed) and nonlinear (localized) pressure losses along the flow path, and must correspond to physiological values under defined inlet flow and pressure conditions. The lumped parameter model (LPM) representation of our mock circulatory loop is illustrated in Fig. 4.7.

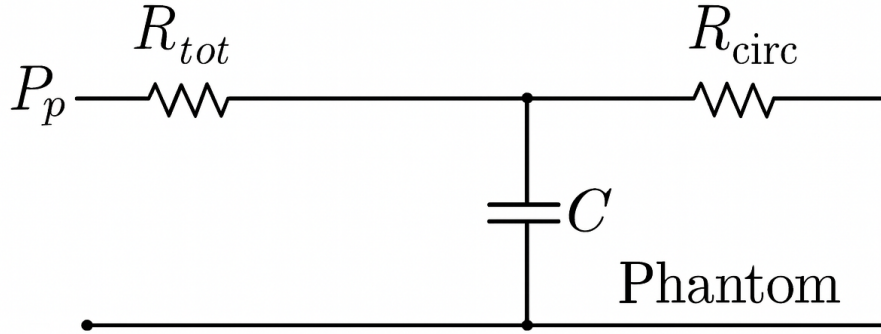


**Figure 4.7: Lumped Parameter Model (LPM) of the Mock Circulatory Loop.** The system includes a proximal pressure source  $P_p$ , a total lumped resistance  $R_{\text{tot}}$ , a distal circulatory resistance  $R_{\text{circ}}$ , and a compliant element  $C$  representing the aortic phantom. The downstream pressure is denoted  $P_{\text{phantom}}$ .

We define the total resistance as:

$$R_{\text{tot}} = R_{\text{dist}}^{\text{asc} \rightarrow \text{ren}} + 2 \cdot R_{\text{dist}}^{\text{ren} \rightarrow \text{iliac}} + R_{\text{curve}} + R_{\text{bif}} + R_{\text{AAA}} \quad (4.4)$$

where the individual terms are described below:

$R_{\text{dist}}^{\text{asc} \rightarrow \text{ren}}$  Distributed (linear) resistance along the aortic segment extending from the ascending aorta to the suprarenal abdominal aorta. This segment is modeled as a straight cylindrical tube under laminar flow assumptions, using the classical Hagen–Poiseuille equation:

$$R = \frac{8\mu L}{\pi r^4}$$

$$L_1 = 0.4 \text{ m}$$

$$r_1 = 0.0125 \text{ m}$$

where  $L$  is the length of the segment,  $r$  its internal radius.

$2 \cdot R_{\text{dist}}^{\text{ren} \rightarrow \text{iliac}}$  Distributed resistance from the suprarenal point to each iliac artery. Since the flow splits symmetrically, both iliac branches contribute equally. The same Poiseuille formulation is used, assuming geometrical similarity between the two branches. The

corresponding length and diameter are as following:

$$L_2 = 0.1 \text{ m}$$

$$r_2 = 0.003 \text{ m}$$

**$R_{\text{curve}}$**  Local (minor) resistance caused by the  $180^\circ$  curvature of the aortic arch. This is characterized by a minor loss coefficient  $K_{\text{curve}}$ , which depends on curvature ratio and Reynolds number. The associated pressure loss is translated to resistance using [46]:

$$R_{\text{curve}} = \frac{K_{\text{curve}} \cdot \rho}{2A^2}$$

For a  $180^\circ$  return bend, the minor loss coefficient K is equal to 0.2.[40]

where  $\rho$  is the fluid density and  $A$  is the cross-sectional area at the curve.

**$R_{\text{bif}}$**  Bifurcation resistance arising from the division of flow at the aortic terminus into the left and right common iliac arteries. The bifurcation angle is approximately  $135^\circ$ , leading to a  $60^\circ$  divergence between branches. This angular geometry induces flow separation and secondary vortices, typically modeled with empirical bifurcation coefficients.

$$R_{\text{Bif}} = \frac{K_{\text{Bif}} \cdot \rho}{2A^2}$$

According to our Geometry, the corresponding K is defined equal to 0.2.[40] The minor loss coefficient  $K = 0.2$  is based on the velocity in the main pipe before the flow divides. Therefore, the area A used in the formula must correspond to the aorta's cross-section before bifurcation, not the branches (iliac arteries).

**$R_{\text{AAA}}$**  Local nonlinear resistance associated with the abdominal aortic aneurysm. The aneurysmal sac causes sudden expansion and contraction of the flow path, leading to turbulence, eddy formation, and energy dissipation. Based on literature, a 30% increase in cross-sectional area may yield a minor loss coefficient  $K_{\text{AAA}} \approx 0.2 - 0.4$ , from which resistance is computed as [46]:

$$R_{\text{AAA}} = \frac{K_{\text{AAA}} \cdot \rho}{2A^2}$$

The reference velocity (and therefore area) is taken before the expansion, where flow enters the aneurysmal sac. Therefore the A in this formula is relative to the original vessel size

**Table 4.6: Analytical Estimation of Individual Resistance Components Considering the Phantom Morphology**

Resistance Component	Value	Units
$R_{\text{dist}}^{\text{asc} \rightarrow \text{ren}}$	101,860	$\text{Pa}\cdot\text{s}/\text{m}^3$
$R_{\text{dist}}^{\text{ren} \rightarrow \text{iliac}}$	6,518,985	$\text{Pa}\cdot\text{s}/\text{m}^3$
$R_{\text{curve}}$	1,013,211	$\text{Pa}\cdot\text{s}/\text{m}^3$
$R_{\text{bif}}$	1,544,294	$\text{Pa}\cdot\text{s}/\text{m}^3$
$R_{\text{AAA}}$	2,026,422	$\text{Pa}\cdot\text{s}/\text{m}^3$
$R_{\text{tot}}$	17,723,757	$\text{Pa}\cdot\text{s}/\text{m}^3$
$R_{\text{tot}}$	0.133	$\text{mmHg}\cdot\text{s}/\text{mL}$

Now that the total resistance of the phantom has been analytically determined, we can estimate the steady-state pressure drop ( $\Delta P$ ) across the system for various physiological flow rates. It is important to note that a pressure drop exceeding 20 mmHg from the ascending to the iliac branches is generally considered indicative of pathological conditions. As shown in Table 4.7, the calculated pressure drops for cardiac outputs ranging from 3 to 8 L/min remain well within this physiological threshold. Despite the geometric complexity and localized high-resistance regions of the phantom — including bifurcation, curvature, and aneurysmal expansions — the system demonstrates hemodynamic fidelity and maintains pressure drops in a clinically acceptable range.

**Table 4.7: Pressure Drop Across the Phantom for Different Cardiac Outputs in steady-state case**

Cardiac Output	$Q$ (mL/s)	$\Delta P$ (mmHg)
3 L/min	50.0	6.65
4 L/min	66.67	8.87
5 L/min	83.33	11.08
6 L/min	100.0	13.3
7 L/min	116.67	15.52
8 L/min	133.33	17.73

The diastolic-decay fit gives an effective characteristic (Windkessel R) resistance of 0.133  $\text{mmHg}\cdot\text{s mL}^{-1}$ . Recent lumped-parameter analyses that coupled CFD to CT-angiography report R values between 0.10 and 0.15  $\text{mmHg}\cdot\text{s mL}^{-1}$  for the brachiocephalic trunk, left common carotid, left subclavian and descending thoracic aorta in 25 paediatric subjects,

fully bracketing the present value[50]. In vivo four-element Windkessel fits obtained in anaesthetised swine yield a closely matching proximal aortic impedance of  $0.105 \pm 0.009$  mmHg·s mL<sup>1</sup>.[22]. Taken together, these data confirm that the resistive component implemented in our prototype is physiologically credible, and further numerical tuning is unwarranted; any additional refinement must therefore rely on direct experimental measurements.

---



## Bibliography

- [1] M. e. a. Arjmandi. Challenges in flexible phantom fabrication: a review. *Journal of Biomedical Materials Research Part B: Applied Biomaterials*, 111:1023–1034, 2023.
- [2] A. P. Avolio, L. Van Bortel, P. Boutouyrie, and et al. Role of pulse pressure amplification in arterial hypertension: Experts' opinion and review of the literature. *Hypertension*, 61(5):1035–1041, 2013. doi: 10.1161/HYPERTENSIONAHA.111.00473.
- [3] R. K. Banerjee, L. H. Back, and M. R. Back. A technique for comparing wall pressure distributions in steady flow through rigid versus flexible patient-based abdominal aortic aneurysm phantoms. *Medical Engineering & Physics*, 77:60–67, 2020. doi: 10.1016/j.medengphy.2020.01.003.
- [4] C. A. Blum, M. Kohn, P. Kunz, P. M. Alonso, W. Blecker, A. A. Platteau, L.-H. Guimaraes, U. Grundemann, D. Leander, J. L. Gordon, and J. Miller. Abdominal aortic aneurysm: pictorial review of common imaging findings. *Annals of Translational Medicine*, 5(8), 2017. doi: 10.21037/atm.2017.04.32. Features illustrative CTA images of intact and ruptured AAAs, mural thrombus, calcification, and complications including aorto-enteric and aorto-caval fistulae.
- [5] M. Boufi, T. Guegan, A. Loundou, A. Pellissier, C. Argenson, and P. Magnan. Morphological analysis of the aortic arch using computed tomography angiography in a healthy population. *European Journal of Vascular and Endovascular Surgery*, 54(3): 365–372, 2017. doi: 10.1016/j.ejvs.2017.06.014.
- [6] M. Boufi, C. Guivier-Curien, A. D. Loundou, V. Deplano, O. Boiron, K. Chaumoitre, V. Gariboldi, and Y. S. Alimi. Morphological Analysis of Healthy Aortic Arch. *European Journal of Vascular and Endovascular Surgery*, 53(5):663–670, 2017. doi: 10.1016/j.ejvs.2017.02.023.
- [7] P. Boutouyrie, B. Berruyer, S. Vermeersch, and S. Laurent. Assessment of aortic distensibility by automatic pulse wave velocity measurement: Validation and application in hypertension. *Hypertension*, 20(2):272–279, 1992. doi: 10.1161/01.HYP.20.2.272.

- [8] W. Chen, X. Li, and Y. Wang. Understanding the hemodynamics of the aortic valve and root. *Journal of Biomechanics*, 55:1–10, 2021.
- [9] C. Clinic. About the aorta – the aorta and its structure, 2023. URL <https://my.clevelandclinic.org/health/body/21175-aorta>. Accessed: 2025-07-02.
- [10] L. Da Vinci. *Anatomical Studies*. 1513. Manuscript, widely published in later editions.
- [11] P. H. Geoghegan, P. Williamson, P. D. Docherty, S. G. Yazdi, M. Jermy, A. Khanafer, and N. Kabaliuk. In vitro pulsatile flow study in compliant and rigid ascending aorta phantoms. *Medical Engineering Physics*, 94:1–11, 2021. doi: 10.1016/j.medengphy.2021.08.010. Compares velocity fields in rigid vs. compliant aortic-arch phantoms under pulsatile flow :contentReference[oaicite:1]index=1.
- [12] C. Gozzo, G. Caruana, R. Cannella, A. Farina, D. Giambelluca, E. Dinoto, F. Vernuccio, A. Basile, and M. Midiri. Ct angiography for the assessment of evar complications: a pictorial review. *Insights into Imaging*, 13(1):5, 2022. doi: 10.1186/s13244-021-01112-4. Includes extensive CTA figures demonstrating aneurysm morphology, intraluminal thrombus, calcification, and stent-graft complications.
- [13] H. B. Grotenhuis, J. J. Westenberg, P. Steendijk, R. J. van der Geest, J. H. Reiber, and A. de Roos. Regional aortic distensibility and pulse wave velocity assessed with magnetic resonance imaging in healthy young adults. *Journal of Magnetic Resonance Imaging*, 30(3):521–528, 2009.
- [14] A. Guala, L. D'Elia, A. F. Gelpi, and et al. In vivo assessment of aortic strain and distensibility in healthy subjects using 4d flow mri. *Frontiers in Cardiovascular Medicine*, 9:850196, 2022. doi: 10.3389/fcvm.2022.850196.
- [15] K. Hayashi, B. Takase, H. Kinjo, and T. Hirose. A simplified model for input impedance of the arterial system. *Journal of Biomechanics*, 12(4):251–259, 1979. Derives arterial compliance using a thin-walled cylindrical approximation, leading to

$$C = \frac{\pi L D_0^3}{4 E t}$$

based on linear elasticity for vessel radius changes under pressure.

- [16] G. A. Holzapfel, T. C. Gasser, and R. W. Ogden. A new constitutive framework for arterial wall mechanics and a comparative study of material models. *Journal of Elasticity and the Physical Science of Solids*, 61(1-3):1–48, 2000. doi: 10.1023/A:1010835316564.

- [17] T. D. Homan, S. Bordes, and E. Cichowski. Physiology, pulse pressure. *StatPearls Publishing LLC*, 2025. “A normal young adult at rest has a stroke volume of approximately 80mL. Arterial compliance is approximately 2mL/mmHg, which confirms that normal pulse pressure is approximately 40mmHg.”
- [18] W. Hong, H. Yu, J. Chen, Z. Liu, and H. Zhou. A mock circulation loop to characterize in vitro hemodynamics in human systemic arteries with stenosis. *Fluids*, 8(7):198, 2023.
- [19] A. Johnson, C. Davies, and E. Miller. Advanced imaging of aortic anatomy and pathology. *Journal of Vascular Medicine*, 15(2):112–125, 2023.
- [20] R. E. Klabunde. *Cardiovascular Physiology Concepts*. Lippincott Williams & Wilkins, a Wolters Kluwer business, Philadelphia, PA, 3 edition, 2022. ISBN 978-1975150075.
- [21] I. Kokalari, B. Lale-Kokalari, N. Filipovic, G. Bijelic, and L. Madjar. A mathematical model of the cardiovascular system for the evaluation of ventricular assist devices. *Scientific Research and Essays*, 8(9):387–404, 2013.
- [22] P. Kolh, V. D’Orio, B. Lambermont, P. Gérard, C. Gommes, and R. Limet. Increased aortic compliance maintains left ventricular performance at lower energetic cost. *European Journal of Cardio-Thoracic Surgery*, 17(3):272–278, 2000. doi: 10.1016/S1010-7940(00)00341-9.
- [23] S. Laurent, P. Boutouyrie, R. Asmar, I. Gautier, B. Laloux, L. Guize, P. Ducimetière, and A. Benetos. Aortic stiffness is an independent predictor of all-cause and cardiovascular mortality in hypertensive patients. *Hypertension*, 37(5):1236–1241, 2001. doi: 10.1161/01.HYP.37.5.1236. Expert consensus also asserts that PWV is inversely related to vascular compliance/distensibility – stiffer vessels transmit waves faster :contentReference[oaicite:2]index=2.
- [24] R. Leloup, R. van Loon, and et al. Combining computational and experimental modeling for cardiovascular research: Challenges and opportunities. *Biomechanics and Modeling in Mechanobiology*, 22:421–437, 2023. doi: 10.1007/s10237-022-01668-7.
- [25] X. Liu, Y. Fan, X. Deng, and F. Zhan. A numerical study of the influence of blood viscosity on pulsatile flows in a stenosed carotid bifurcation. *Journal of Biomechanics*, 40(10):2262–2270, 2007.
- [26] M. Markl, A. Frydrychowicz, S. Kozerke, M. Hope, and O. Wieben. 4d flow mri. *Journal of Magnetic Resonance Imaging*, 49(4):945–962, 2019. doi: 10.1002/jmri.26644.

- [27] W. W. Nichols, M. F. O'Rourke, and C. Vlachopoulos. *McDonald's Blood Flow in Arteries: Theoretical, Experimental and Clinical Principles*. CRC Press, 6th edition, 2011.
- [28] C. A. Nienaber and R. E. Clough. Management of acute aortic dissection. *The Lancet*, 385(9970):800–811, 2015. doi: 10.1016/S0140-6736(14)61005-9.
- [29] N. e. a. Okamoto. Vascular stiffness in aging and disease. *Frontiers in Cardiovascular Medicine*, 2022. URL <https://www.ncbi.nlm.nih.gov/pmc/articles/PMC8688960/>.
- [30] L. P. Parker, F. Fiusco, F. Rorro, L. Formaggia, F. Migliavacca, M. Biffi, and S. Ippolito. Venovenous extracorporeal membrane oxygenation drainage cannula performance: From generalized to patient-averaged vessel model. *Physics of Fluids*, 36(6):067113, 2024.
- [31] R. A. Peattie, E. Golden, R. S. Nomoto, C. M. Margossian, F. Q. Pancheri, E. S. Edgar, M. D. Iafrati, and A. L. Dorfmann. A technique for comparing wall pressure distributions in steady flow through rigid versus flexible patient-based abdominal aortic aneurysm phantoms. *Experimental Techniques*, 40(5):1187–1201, 2016. doi: 10.1007/s40799-016-0119-4. Utilizes rigid and effectively rigid thick-wall AAA phantoms to assess differences in wall pressure distributions :contentReference[oaicite:2]index=2.
- [32] A. Redheuil, D. C. Yu, P. M. Mousseaux, and J. A. Lima. Age-related changes in aortic arch geometry: Relationship with proximal aortic function and left ventricular mass and remodeling. *Journal of the American College of Cardiology*, 58(12):1262–1270, 2010. doi: 10.1016/j.jacc.2011.06.015.
- [33] L. M. Resnick et al. Direct magnetic resonance determination of aortic distensibility in essential hypertension: Relation to age, abdominal visceral fat, and in situ intracellular free magnesium. *Hypertension*, 30(3):654–660, 1997. doi: 10.1161/01.HYP.30.3.654. Used cardiac MRI to measure cross-sectional aortic area changes during systole and diastole and calculate distensibility from pulse pressure :contentReference[oaicite:1]index=1.
- [34] R. Scicolone, K. I. Paraskevas, G. Argiolas, A. Balestrieri, P. Siotto, J. S. Suri, M. Porcu, C. Mantini, M. Caulo, S. Masala, F. Cademartiri, R. Sanfilippo, and L. Saba. Atherosclerotic abdominal aortic aneurysms on computed tomography angiography: A narrative review on spectrum of findings, structured reporting, treatment, secondary complications and differential diagnosis. *Diagnostics*, 14(5):682,

2024. doi: 10.3390/diagnostics14050682. URL <https://www.mdpi.com/2075-4418/14/5/682>.
- [35] P. Segers, N. Stergiopoulos, M. Madani, and P. Verdonck. Systemic pulse pressure: re-evaluation of its determinants by a model-based approach. *Hypertension*, 37(4): 1094–1100, 2001.
  - [36] L. Smith and R. Jones. Comprehensive review of cardiac anatomy and physiology. *Cardiology Today*, 28(1):45–60, 2024.
  - [37] C. Stefanadis, H. Tsiamis, C. Vlachopoulos, and P. Toutouzas. Pressure-volume relationship of the human aorta: A new method of evaluation by means of the intra-coronary balloon technique. *Circulation*, 88(2):417–426, 1993. doi: 10.1161/01.CIR.88.2.417.
  - [38] N. Stergiopoulos, B. Westerhof, and N. Westerhof. Total arterial inertance as the fourth element of the windkessel model. *American Journal of Physiology-Heart and Circulatory Physiology*, 276(1):H81–H88, 1999.
  - [39] L. Stoiber, N. Ghorbani, M. Kelm, S. Kelle, et al. Validation of simple measures of aortic distensibility based on standard 4-chamber cine cmr: a new approach for clinical studies. *Clinical Research in Cardiology*, 109:454–464, 2020. doi: 10.1007/s00392-019-01525-8. Demonstrated reproducible distensibility assessment from cine CMR, including diameter- and area-based methods :contentReference[oaicite:2]index=2.
  - [40] The Engineering Toolbox. Minor loss coefficients in pipe components, n.d. URL [https://www.engineeringtoolbox.com/minor-loss-coefficients-pipes-d\\_626.html](https://www.engineeringtoolbox.com/minor-loss-coefficients-pipes-d_626.html). Accessed: 2025-06-29.
  - [41] B. Trachet, A. Piersigilli, and et al. A new method for in vitro assessment of aortic biomechanics: validation using ex vivo porcine aortas and comparison with in vivo human data. *Annals of Biomedical Engineering*, 49:1541–1553, 2021. doi: 10.1007/s10439-021-02718-y.
  - [42] I. Voges, M. Jerosch-Herold, J. Hedderich, E. Pardun, C. Hart, D. D. Gabbert, J. Hansen, M. Stöckel, A.-C. Jenke, and H.-H. Kramer. Normal values of aortic dimensions, distensibility, and pulse wave velocity in children and young adults: a cross-sectional study using cardiovascular magnetic resonance. *Journal of Cardiovascular Magnetic Resonance*, 14(1):1–11, 2012.
  - [43] J. E. Wagenseil and R. P. Mecham. Elastin in large artery stiffness and hypertension.

- Journal of Cardiovascular Translational Research*, 11:258–267, 2018. doi: 10.1007/s12265-018-9812-0.
- [44] X. e. a. Wang. Impact of environmental conditions on flexible phantom quality. *Journal of Mechanics in Medicine and Biology*, 22, 2022.
  - [45] N. Westerhof, J. Lankhaar, and B. Westerhof. The arterial windkessel. *Medical & Biological Engineering & Computing*, 47:131–141, 2009.
  - [46] F. M. White. *Fluid Mechanics*. McGraw-Hill Education, New York, 7 edition, 2011.
  - [47] S. Williams, J. Brown, and M. Green. The aortic root: Structure, function, and clinical implications. *Circulation Research*, 130(7):1001–1015, 2022.
  - [48] K.-W. Xu, Q. Gao, M. Wan, and K. Zhang. Mock circulatory loop applications for testing cardiovascular assist devices and in vitro studies. *Frontiers in Physiology*, 14: 1175919, 2023.
  - [49] S. G. Yazdi, L. Huetter, P. D. Docherty, P. N. Williamson, D. Clucas, M. Jermy, and P. H. Geoghegan. A novel fabrication method for compliant silicone phantoms of arterial geometry for use in particle image velocimetry of haemodynamics. *Applied Sciences*, 9(18):3811, 2019. doi: 10.3390/app9183811. Notes challenges like variable wall thickness ( $0.815\text{mm} \rightarrow 0.317\text{mm}$ ) and surface roughness due to dip-coating and mold design in silicone aortic phantoms :contentReference[oaicite:1]index=1.
  - [50] Y. Zhu, R. Chen, Y.-H. Juan, H. Li, J. Wang, Z. Yu, and H. Liu. Clinical validation and assessment of aortic hemodynamics using computational fluid dynamics simulations from computed tomography angiography. *BioMedical Engineering OnLine*, 17 (1):53, 2018. doi: 10.1186/s12938-018-0485-5.

# A

## Appendix A: Governing C<sub>1</sub> and C<sub>2</sub> from the uniaxial test

### Appendix A: Fitting Mooney–Rivlin Constants to Uniaxial Test Data

To determine the material constants  $C_1$  and  $C_2$  for the Mooney–Rivlin hyperelastic model, five uniaxial tensile tests were performed on identical material specimens. The engineering stress–stretch data were fitted using Microsoft Excel.

#### Uniaxial Stretch Formulation

For incompressible isotropic materials under uniaxial tension, the Cauchy (true) stress is given by:

$$\sigma_{\text{true}} = 2 \left[ C_1 \left( \lambda^2 - \frac{1}{\lambda} \right) + C_2 \left( \lambda - \frac{1}{\lambda^2} \right) \right]$$

Experimental data, however, are reported in terms of *engineering stress*, which relates to the true stress by:

$$\sigma_{\text{eng}} = \frac{\sigma_{\text{true}}}{\lambda}$$

Substituting, the final expression used for fitting is:

$$\sigma_{\text{eng}} = \left[ 2C_1 + \frac{2C_2}{\lambda} \right] \left( \lambda - \frac{1}{\lambda^2} \right) \quad (1)$$

## Parameter Extraction

Five repeated uniaxial-tension experiments were performed on strips excised from the same silicone batch used to cast the aortic phantom. Axial stretch and the corresponding engineering stress were recorded over the physiological deformation range, and all stress–stretch data were pooled and fitted simultaneously with the two-parameter Mooney–Rivlin model in Microsoft Excel Solver.

Equation (1) was implemented in Excel, and the parameters  $C_1$  and  $C_2$  were optimized by minimizing the squared error between the model and the experimental data. The best-fit constants obtained were:

$$C_1 = 0.022318 \text{ MPa}$$

$$C_2 = 0.016764 \text{ MPa}$$

These parameters were subsequently used in the analytical and numerical models of the aortic phantom described in the main body of this thesis.

# List of Figures

2.1	<b>Anatomical structure of the aorta</b> , including the ascending aorta, aortic arch, descending thoracic aorta, and vessel wall layers (intima, media, and adventitia)[9] . . . . .	6
2.2	Classification of abdominal aortic aneurysms (AAAs) by location. (1) <i>Normal aorta</i> , (2) <i>Infrarenal</i> (3) <i>Short-neck infrarenal</i> (4) <i>Juxtarenal</i> (5) <i>Pararenal</i> (involves renal arteries), (6) <i>Paravisceral</i> (involves renal arteries and SMA) [34]. . . . .	11
2.3	Anatomical classification of aortic dissection based on the DeBakey and Stanford systems. Adapted from Nienaber and Clough [28]. . . . .	12
2.4	functions of different blood vessels [20] . . . . .	14
3.1	Windkessel models commonly used in lumped parameter cardiovascular simulations. (a) Two-element model consisting of a resistor and a capacitor. (b) Classical three-element Windkessel model introduced by Westerhof et al. with proximal impedance $Z_c$ . (c) Modified 3-element configuration with $Z_c$ in series[21]. . . . .	29
3.2	Example of a multi-compartment lumped parameter model representing the systemic circulation. The diagram includes the aorta ( $C_{ao}$ , $R_{ao}$ , $L_{ao}$ ), arteries, arterioles and capillaries, and veins, each represented by combinations of resistive ( $R$ ), capacitive ( $C$ ), and inertive ( $L$ ) elements[21]. . . . .	30
3.3	Lumped parameter model representing the circulatory loop including sensor resistance ( $R_{\text{sensor}}$ ), phantom inlet resistance ( $R_{\text{ph}}$ ), flow resistance ( $k$ ), compliance ( $C_{\text{phantom}}$ ), and downstream arterial resistance ( $R_{\text{circ}}$ ). . . . .	31
3.4	Circulatory Blood pressure(From Left ventricle to Vena Cava)[20] . . . . .	37
3.5	<b>Initial 3D model of the full aorta with all major branches.</b> Segmented from contrast-enhanced CT images using a multi-mask approach. .	38
3.6	<b>Cleaned and trimmed aortic model used in the physical phantom.</b> Non-essential branches were removed . . . . .	39
3.7	Standardized morphological parameters and reference planes of the aortic arch, adapted from [6]. . . . .	40

3.8	<b>3D-printed aortic phantom.</b> Directly printed in hyperelastic VisiJet CE elastomer on a high-resolution MJP printer at SanDonato Hospital. . . . .	43
4.1	Compliance of the aortic phantom as a function of physiological pressure for various external water heights. . . . .	49
4.2	Volumetric distensibility ( $D_v$ ) of the aortic phantom as a function of physiological arterial pressure ( $P_{in}$ ) at various external water heights. . . . .	51
4.3	Circumferential strain as a function of internal pressure under different external water heights . . . . .	53
4.4	<b>Complete mock circulatory loop.</b> The system includes the pressurizable compliance box housing the aorta phantom, inlet and outlet tubing, valves (Taps 1–5), a volumetric-flow pump, and connection points for pressure sensors. The layout enables control of fluid flow, adjustment of chamber water level. . . . .	54
4.5	Inelt and Outlet of box, Including the connection tubes . . . . .	56
4.6	<b>Lid and Clamp Assembly for the Compliance Chamber.</b> The lid is secured to the top clamp using uniformly distributed M5 screws. An O-ring with a 5 mm cross-section is placed in a filleted groove to prevent sharp-edge contact and ensure airtight sealing under pressure. The bottom clamp is permanently glued to the box and serves as a structural interface for the lid. . . . .	58
4.7	<b>Lumped Parameter Model (LPM) of the Mock Circulatory Loop.</b> The system includes a proximal pressure source $P_p$ , a total lumped resistance $R_{tot}$ , a distal circulatory resistance $R_{circ}$ , and a compliant element $C$ representing the aortic phantom. The downstream pressure is denoted $P_{phantom}$ . . . . .	60

# List of Tables

2.1 Representative Aortic Distensibility Values ( $\times 10^{-3}\text{mmHg}^{-1}$ ) by Aortic Segment and Sex in Healthy Subjects[42]. . . . .	19
3.1 Published Experimental Data for Human Systemic Arterial Vasculature Models . . . . .	35
3.2 Morphometric and geometric parameters of the healthy aortic arch (mean $\pm$ SD), adapted from [6]. . . . .	42
4.1 List of Parameters Used in MATLAB-Based Parametric Analysis	48
4.2 Physiological Aortic Distensibility Values from Literature . . . . .	51
4.3 Components of the Experimental Setup . . . . .	55
4.4 Components of the Experimental Setup for Aorta Phantom Testing. . . . .	55
4.5 Connection Ports of the Compliance Chamber refering Figure 4.5 . . . . .	57
4.6 Analytical Estimation of Individual Resistance Components Considering the Phantom Morphology . . . . .	62
4.7 Pressure Drop Across the Phantom for Different Cardiac Outputs in steady-state case . . . . .	62



# Acknowledgements

First and foremost, I would like to express my deepest gratitude to everyone who has shown me kindness, support, and encouragement throughout this journey.

I am profoundly thankful to my advisor, Prof. Votta, whose continuous support, guidance, and belief in me have made this thesis possible. Thank you for being not just a mentor but a steady hand when things became uncertain.

To my friends, thank you for standing by me, for the laughter and companionship, and for reminding me to take a breath when I forgot to. Each of you holds a special place in this chapter of my life.

And then, to the most intimate and sacred part of my world—my family. Words are not enough to describe the depth of my love and gratitude for you. Every effort, every sleepless night, every word written in this thesis has been devoted to you. Your love has been my anchor, your faith in me my light. I owe everything I am to your unwavering support.

